

AD-A061 039

ARMY ENGINEER WATERWAYS EXPERIMENT STATION VICKSBURG MISS F/6 13/2  
LIQUEFACTION POTENTIAL OF DAMS AND FOUNDATIONS. REPORT 5. DEVEL--ETC(U)  
AUG 78 G Y BALADI, B ROHANI

UNCLASSIFIED

WES-RR-5-76-2-5

NL

1 OF 1  
AD  
A061039



AD AU 61039

DDC FILE COPY



LEVEL II

14 WES'-RR-

RESEARCH REPORT S-76-2-5



12

5

LIQUEFACTION POTENTIAL OF DAMS AND FOUNDATIONS •

Report 5 •

DEVELOPMENT OF A CONSTITUTIVE RELATION FOR SIMULATING THE RESPONSE OF SATURATED COHESIONLESS SOIL •

by

George Y. Baladi / Behzad Rohani

Geotechnical Laboratory

U. S. Army Engineer Waterways Experiment Station

P. O. Box 631, Vicksburg, Miss. 39180

Research Rept.  
Sep 76 - Aug 77

August 1978

Report 5 of a Series

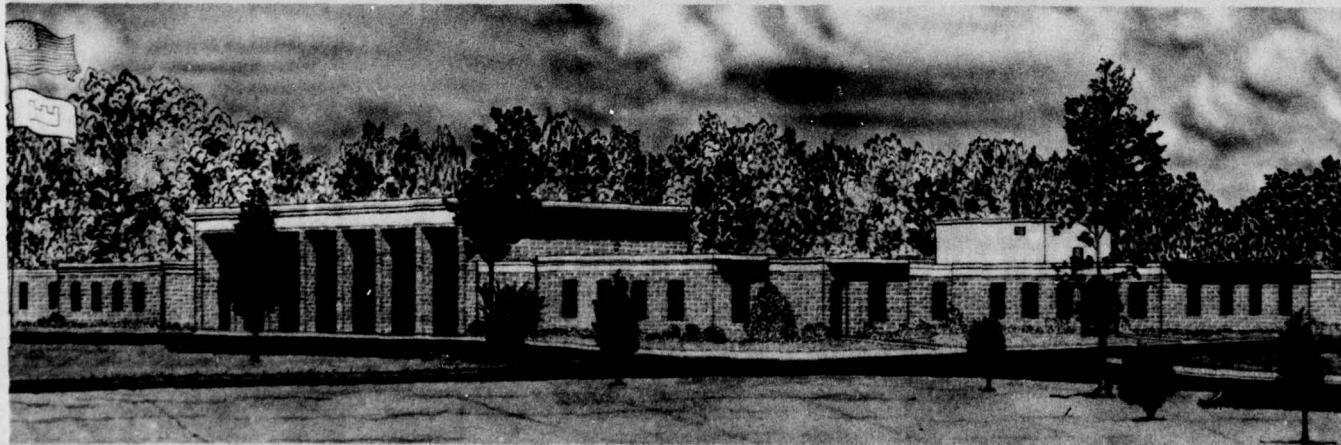
64 p.

DDC

RECEIVED  
NOV 08 1978

E

Approved For Public Release; Distribution Unlimited



Prepared for Office, Chief of Engineers, U. S. Army  
Washington, D. C. 20314

Under CWIS 31145

038100  
78 10 31 061

1/B

Destroy this report when no longer needed. Do not return  
it to the originator.



# LEVEL II

12

Unclassified

SECURITY CLASSIFICATION OF THIS PAGE (When Data Entered)

REPORT DOCUMENTATION PAGE		READ INSTRUCTIONS BEFORE COMPLETING FORM
1. REPORT NUMBER Research Report S-76-2 ✓	2. GOVT ACCESSION NO.	3. RECIPIENT'S CATALOG NUMBER
4. TITLE (and Subtitle) LIQUEFACTION POTENTIAL OF DAMS AND FOUNDATIONS; Report 5, DEVELOPMENT OF A CONSTITUTIVE RELATION FOR SIMULATING THE RESPONSE OF SATURATED COHESIONLESS SOIL		5. TYPE OF REPORT & PERIOD COVERED Report 5 of a series
7. AUTHOR(s) George Y. Baladi Behzad Rohani		6. PERFORMING ORG. REPORT NUMBER
9. PERFORMING ORGANIZATION NAME AND ADDRESS U. S. Army Engineer Waterways Experiment Station Geotechnical Laboratory P. O. Box 631, Vicksburg, Miss. 39180		8. CONTRACT OR GRANT NUMBER(s)
11. CONTROLLING OFFICE NAME AND ADDRESS Office, Chief of Engineers, U. S. Army Washington, D. C. 20314		10. PROGRAM ELEMENT, PROJECT, TASK AREA & WORK UNIT NUMBERS CWIS 31145
14. MONITORING AGENCY NAME & ADDRESS (If different from Controlling Office)		12. REPORT DATE August 1978
		13. NUMBER OF PAGES 59
		15. SECURITY CLASS. (of this report) Unclassified
		15a. DECLASSIFICATION/DOWNGRADING SCHEDULE
16. DISTRIBUTION STATEMENT (of this Report)  Approved for public release; distribution unlimited.		
17. DISTRIBUTION STATEMENT (of the abstract entered in Block 20, if different from Report)		
18. SUPPLEMENTARY NOTES		
19. KEY WORDS (Continue on reverse side if necessary and identify by block number) Cohesionless soils                      Liquefaction (Soils) Constitutive models                    Saturated soils Dams    Stress-strain relations Foundations Hysteresis		
20. ABSTRACT (Continue on reverse side if necessary and identify by block number) This report documents the development of a three-dimensional elastic-plastic isotropic constitutive model for earth materials and demonstrates its ability to simulate a wide variety of observed stress-strain-pore pressure responses of fully saturated cohesionless soils. The model reproduces the hysteretic behavior exhibited by these materials when tested under hydrostatic and deviatoric states of stress, and accounts for shear-induced volume changes, strain-softening response, and progressive increases in pore pressure due to subfailure cyclic loadings. (Continued)		

DDC  
RECEIVED  
NOV 08 1978  
E

CONT' →

DD FORM 1 JAN 73 1473 EDITION OF 1 NOV 65 IS OBSOLETE

Unclassified

SECURITY CLASSIFICATION OF THIS PAGE (When Data Entered)

78 10 31 061



**SECURITY CLASSIFICATION OF THIS PAGE(When Data Entered)**

## 625

7

ACCESSION for		
NTIS	White Section	<input checked="" type="checkbox"/>
DDC	Buff Section	<input type="checkbox"/>
UNANNOUNCED		<input type="checkbox"/>
JUSTIFICATION		
BY		
DISTRIBUTION/AVAILABILITY CODES		
Dist.	GROUP	SUBGROUP
A		

SECURITY CLASSIFICATION OF THIS PAGE(When Data Entered)

## PREFACE

This investigation was conducted at the U. S. Army Engineer Waterways Experiment Station (WES) under the sponsorship of the Office, Chief of Engineers, Department of the Army, as a part of Project CWIS 31145, "Liquefaction Potential of Dams and Foundations Under Earthquake Excitation."

The investigation was conducted by Drs. G. Y. Baladi and B. Rohani during the period September 1976 through August 1977, under the general direction of Mr. J. P. Sale, Chief, Soils and Pavements Laboratory, and Drs. J. G. Jackson, Jr., Chief, Soil Dynamics Division, F. G. McLean, Chief, Earthquake Engineering and Vibrations Division (EE&VD), and W. F. Marcuson III, Project Leader (EE&VD). The report was written by Drs. Baladi and Rohani.

COL J. L. Cannon, CE, was Director of WES during the preparation of this report. Technical Director was Mr. ~~F.~~ R. Brown.

# CONTENTS

	<u>Page</u>
PREFACE . . . . .	1
PART I: INTRODUCTION . . . . .	3
Background . . . . .	3
Purpose . . . . .	4
Scope . . . . .	4
PART II: TYPICAL MECHANICAL BEHAVIOR OF SATURATED COHESIONLESS SOILS . . . . .	5
Behavior Under Monotonic-Type Loading . . . . .	6
Behavior Under Cyclic Loading . . . . .	8
PART III: FORMULATION OF THE CONSTITUTIVE MODEL . . . . .	14
Elastic Behavior . . . . .	15
Plastic Behavior . . . . .	18
Parameter R and Its Effect on Behavior of Model . . . . .	20
PART IV: BEHAVIOR OF THE MODEL UNDER TRIAXIAL TEST CONDITIONS . . . . .	23
Isotropic Consolidation Phase . . . . .	24
Shear Phase . . . . .	26
PART V: COMPARISON OF LABORATORY TEST DATA WITH MODEL PREDICTION . . . . .	34
Material Constants . . . . .	34
Comparison with Contractive Material (Data Set 1) . . . . .	35
Comparison with Dilative Material (Data Set 2) . . . . .	35
Comparison with Strain-Softening Behavior (Data Set 3) . . . . .	38
Comparison with Cyclic Test Results (Data Set 4) . . . . .	42
PART VI: SUMMARY AND RECOMMENDATIONS . . . . .	45
REFERENCES . . . . .	46
TABLE 1	
APPENDIX A: FUNDAMENTAL EQUATIONS OF ELASTIC-PLASTIC MATERIAL MODELS . . . . .	A1
Basic Concepts from Continuum Mechanics . . . . .	A1
General Description of Elastic-Plastic Constitutive Models . . . . .	A3
APPENDIX B: NOTATION . . . . .	B1



LIQUEFACTION POTENTIAL OF DAMS AND FOUNDATIONS  
DEVELOPMENT OF A CONSTITUTIVE RELATION FOR SIMULATING  
THE RESPONSE OF SATURATED COHESIONLESS SOIL

PART I: INTRODUCTION

Background

1. During 1975 a research effort was initiated at the U. S. Army Engineer Waterways Experiment Station (WES) to develop an analytical tool for studying the liquefaction potential of dams and foundations subjected to earthquake excitation. Specifically, the objective was to develop a rational computational method (based on continuum mechanics precepts) for the performance of effective stress analyses of realistically posed boundary-value problems involving fully saturated cohesionless soils.\*

2. The investigation was divided into three phases. Phase I, completed in 1976,<sup>1</sup> involved the development of a three-dimensional (3D) elastic-plastic isotropic constitutive model that qualitatively simulated some of the basic stress-strain-pore pressure response features observed in laboratory tests conducted on fully saturated cohesionless soils. This model, however, does not treat observed strain-softening behavior, nor does it predict the progressive increases in pore pressure observed under low-amplitude (subfailure) cyclic shear loading conditions--two phenomena considered important contributors to the liquefaction problems. These two features were successfully modeled during Phase II of the investigation by appropriate extensions of the Phase I constitutive model. The objective of Phase III (not yet begun) is to incorporate the Phase II version of the constitutive model into a suitable numerical code for future use in the conducting of

---

\* The terms "cohesionless soil" and "sand" are used interchangeably throughout this report to designate earth materials with negligible cohesion.

effective-stress analyses and assessment of liquefaction potential of various earth structures subjected to earthquake or other dynamic loading conditions.

#### Purpose

3. The purpose of this report is to document the results of Phase II of the investigation, i.e., the extension of the Phase I model to (a) include strain-softening shear behavior and (b) predict the progressive increase of pore pressure observed when a saturated sand is subjected to undrained cyclic shear loadings.

#### Scope

4. The typical mechanical behavior of saturated cohesionless soils subjected to various laboratory test loading conditions is discussed in Part II. Part III presents the mathematical formulation of the constitutive model. The behavior of the constitutive model under simulated triaxial test conditions is demonstrated in Part IV. Part V presents comparisons of model predictions with the measured laboratory response of two sands. A summary and recommendations are given in Part VI. Appendix A contains a derivation of the fundamental equations of elastic-plastic constitutive models and is included for reference purposes and future use.

PART II: TYPICAL MECHANICAL BEHAVIOR OF SATURATED  
COHESIONLESS SOILS

5. The mechanical response of a cohesionless soil when subjected to externally applied loads is a function of the volumetric and deviatoric stress-strain properties of the material. These properties, in turn, are affected by such factors as void ratio, density, degree of saturation, interstitial pore fluid, and the loading history of the material. Density, in particular, has a strong influence on the response of the material. Loose sand, for example, contracts and exhibits a ductile-type stress-strain behavior when subjected to a deviatoric state of stress, whereas dense sand dilates and exhibits a brittle-type stress-strain behavior when subjected to a similar stress condition. The boundary between these loose and dense states is characterized by that density at which shearing deformation occurs without volume change. This density is usually referred to as the "critical density," and, as shown in Figure 1,\* its magnitude varies with mean normal stress.<sup>2</sup> The

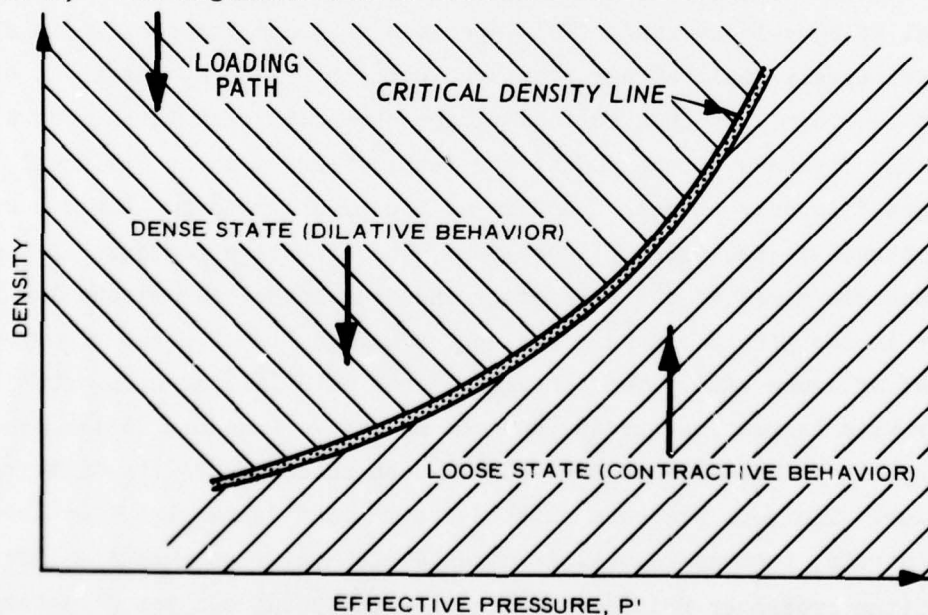


Figure 1. Volumetric response of sand in dense and loose states subjected to a deviatoric state of stress (constant  $P'$ )

\* For convenience, symbols are listed and defined in the Notation (Appendix B).



stress-strain behavior of sand is, therefore, highly dependent on the confining pressure. For fully saturated sand, the stress-strain behavior also varies greatly depending on whether the sand is loaded in a drained or undrained condition. Since the pore fluid (water) is relatively incompressible, pressure builds up in the pore fluid during undrained loading. Consequently, the effective stress carried by the particles comprising the soil skeleton equals the total stress minus this pore pressure. This effective confining pressure, then, influences the undrained stress-strain behavior of saturated sand.

#### Behavior Under Monotonic-Type Loading

6. Figure 2 qualitatively depicts typical stress-strain-pore pressure response curves for four specimens of saturated sand, each at a different initial density, tested undrained in a triaxial test device. As indicated in Figure 2, the specimens are consolidated to the same effective pressure (point 1). The curves marked "1 → 2" show behavior typical of very loose sand. This specimen develops its peak strength at a relatively small strain (compared with the value of strain at the end of the test) and then softens (loses strength) with further straining. The strength at the end of the test, referred to as "residual strength," is only a small fraction of the peak strength. Because of the contractive behavior of loose sand, the effective pressure in the specimen decreases as the test progresses causing a concomitant increase in the pore pressure. The curves marked "1 → 5" show behavior typical of dense sand. The strength of the material increases continuously with increasing strain, and the effective pressure in the dense sand specimen increases as the test is continued, due to its dilative behavior. The pore pressure reaches its maximum value at a relatively small strain, then decreases, eventually becoming less than its initial value (the crossover point occurring when the total and the effective stress paths intersect).

7. Within the extreme limits of very loose and very dense sands a multiplicity of behavior can be observed, depending on the initial

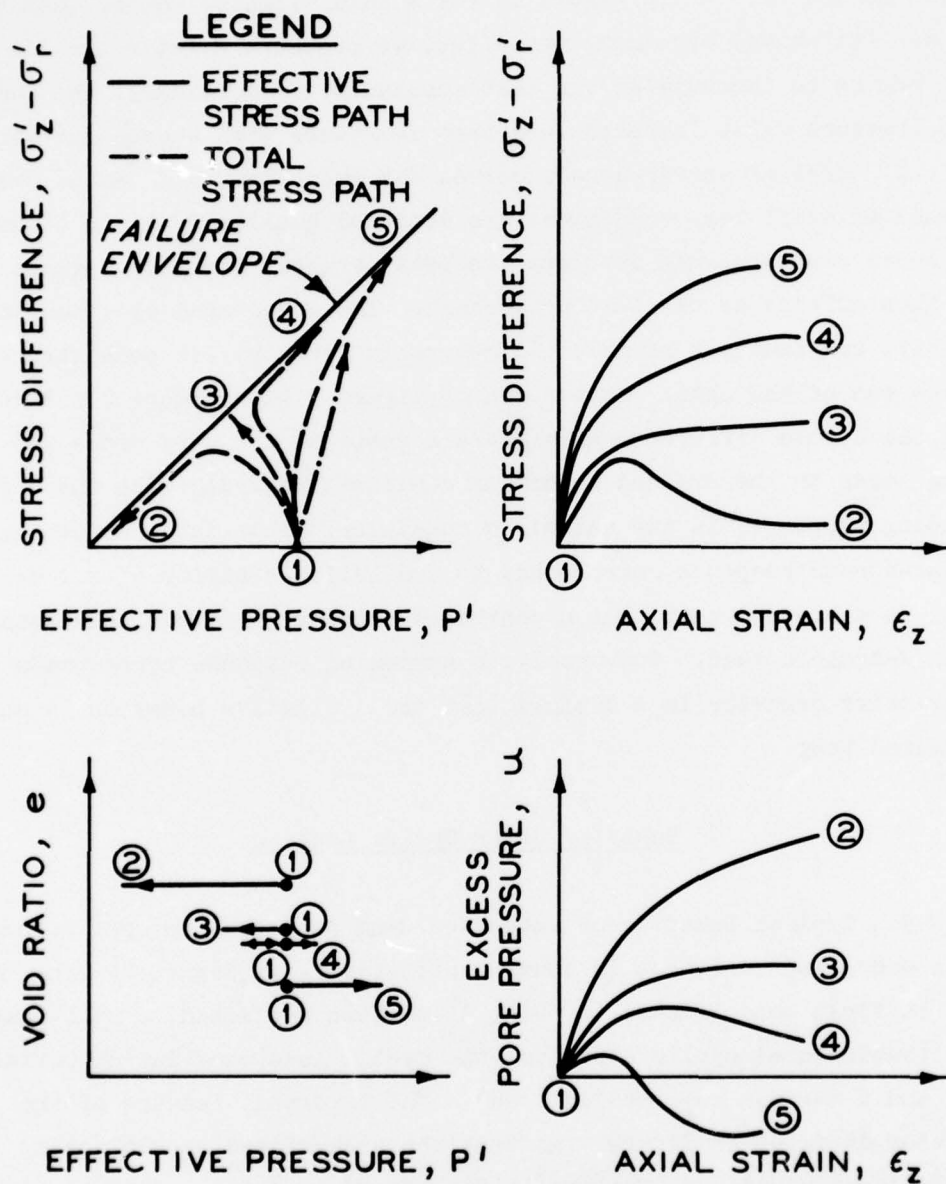


Figure 2. Typical behavior of saturated sand during undrained shear in a triaxial test device

state of compaction of the material. For example, as indicated by the curves marked "1 → 4" in Figure 2, for a sand slightly looser than the densest (dilative) specimen, the effective pressure first decreases and then begins to increase as the test continues. Accordingly, the induced pore pressure first increases and then decreases with increasing strain.

8. Typical stress-strain curves for saturated sand tested under drained triaxial test conditions are depicted qualitatively in Figure 3. The dense sand specimen develops its peak strength early in the test and then softens as the test progresses. The loose sand specimen, conversely, continuously hardens and generally develops its peak strength at the end of the test. Comparison of Figure 3 with Figure 2 indicates that the stress difference-axial strain response for very dense and very loose sands in the drained condition contrasts markedly with the corresponding responses in the undrained condition. That is, a softening stress-strain response corresponds to a dilative behavior (i.e., dense sand) in a drained test, but a contractive behavior (i.e., loose sand) in an undrained test. Conversely, a hardening response corresponds to a contractive behavior in a drained test and a dilative behavior in an undrained test.

#### Behavior Under Cyclic Loading

9. Typical behavior of saturated sand subjected to cyclic loading in an undrained condition is shown qualitatively in Figure 4. The material is first consolidated to point A and then subjected to small amplitude (subfailure) cyclic stresses (the cyclic load oscillating between zero and a maximum compression load). The important feature of the behavior depicted in Figure 4 is that the accumulated strain during cyclic loading prior to failure (point A → B) is small, compared with the strain at the end of the test, whereas the pore pressure increases rapidly during this period. During the last cycle when the effective stress path reaches the failure envelope (point B), the material fails suddenly and loses strength as the test continues (point B → C). The response of the material from point B to point C is similar to the



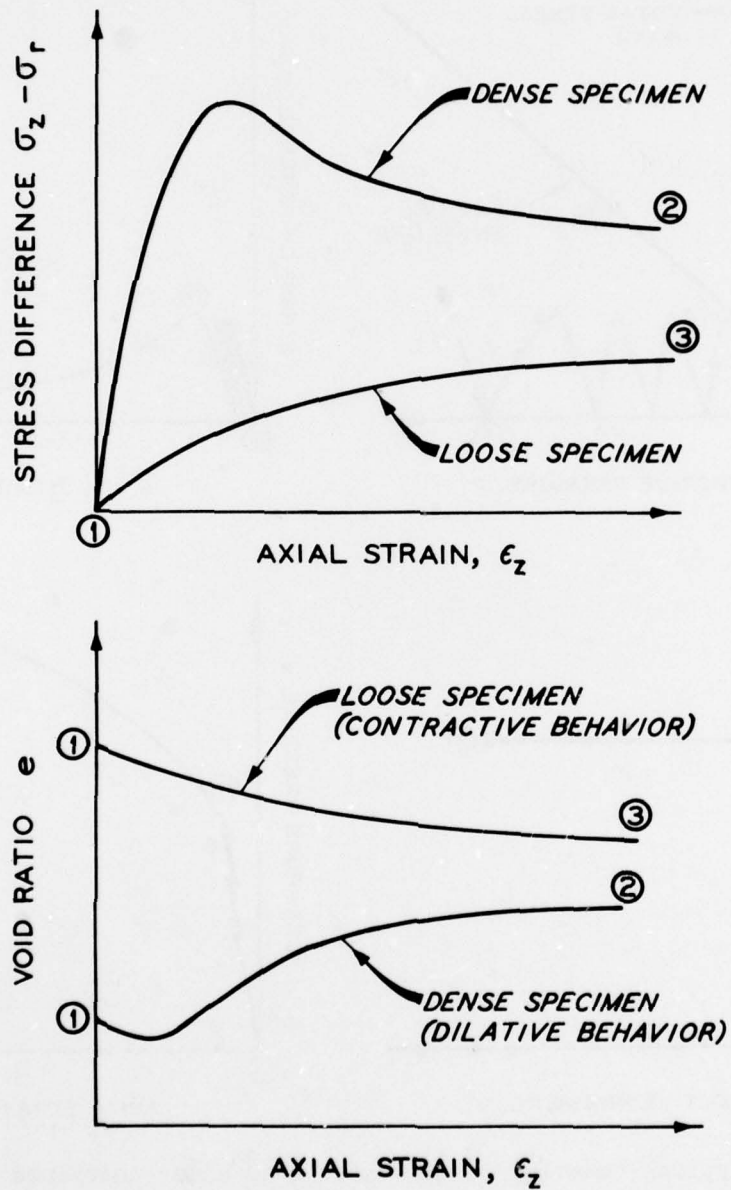


Figure 3. Typical behavior of saturated sand during drained shear in a triaxial test device

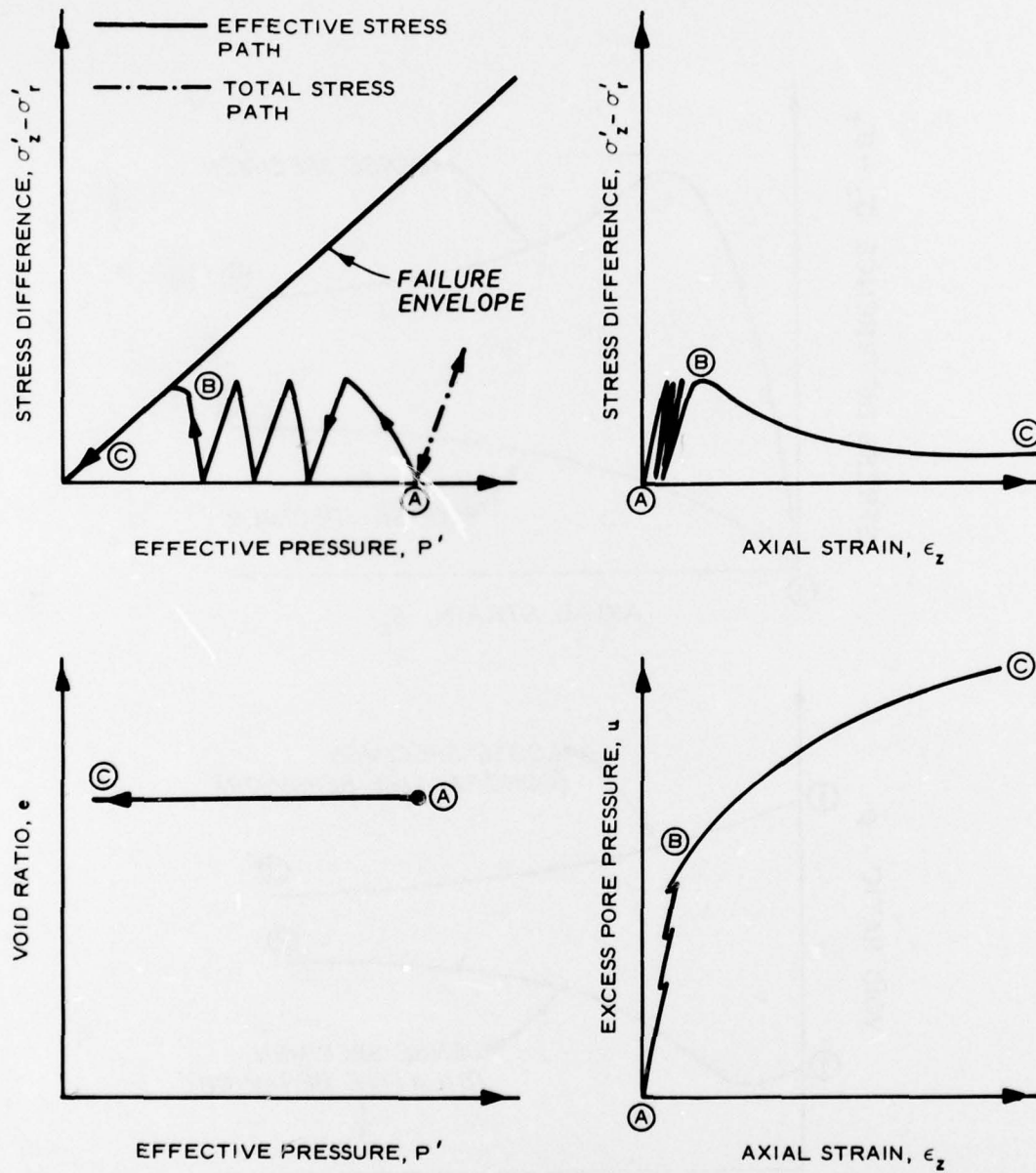


Figure 4. Typical behavior of saturated sand under undrained conditions subjected to cyclic loading in a triaxial test device

response of loose sand under monotonic loading (curves 1 → 2, Figure 2); i.e., the pore pressure increases steadily and reaches its maximum value at point C. At point C the shearing strength of the material is only a small fraction of the strength at point B.

10. Figure 5 portrays typical response of saturated sand in an undrained condition subjected to cyclic stresses with stress reversals (the cyclic load oscillating between a maximum extension and a maximum compression load). The most important feature of the behavior shown in Figure 5 is also similar to that indicated in Figure 4. The accumulated strain prior to failure (point A → B) is very small, but the pore pressure increases rapidly during this period. At point B the material fails suddenly and loses strength with further straining while the pore pressure increases steadily (point B → C).

11. The behavior of loose saturated sand in a drained condition subjected to cyclic shear stresses with stress reversals is shown qualitatively in Figure 6. The rate of volume change decreases as the test progresses; i.e., most of the volumetric strain takes place in the first few cycles of loading. This behavior reflects the rate of pore pressure generation in the corresponding undrained test. Furthermore, the volumetric strain in the first few cycles is plastic (irrecoverable) in nature and becomes mostly elastic in the subsequent cycles. Also, as indicated in Figure 6, the hysteresis loop generated during shear is greatest in the first cycle of loading and becomes smaller as the test continues. Such behavior indicates that during a cyclic drained test, the response of the sand approaches that of an elastic material with the progression of the test.



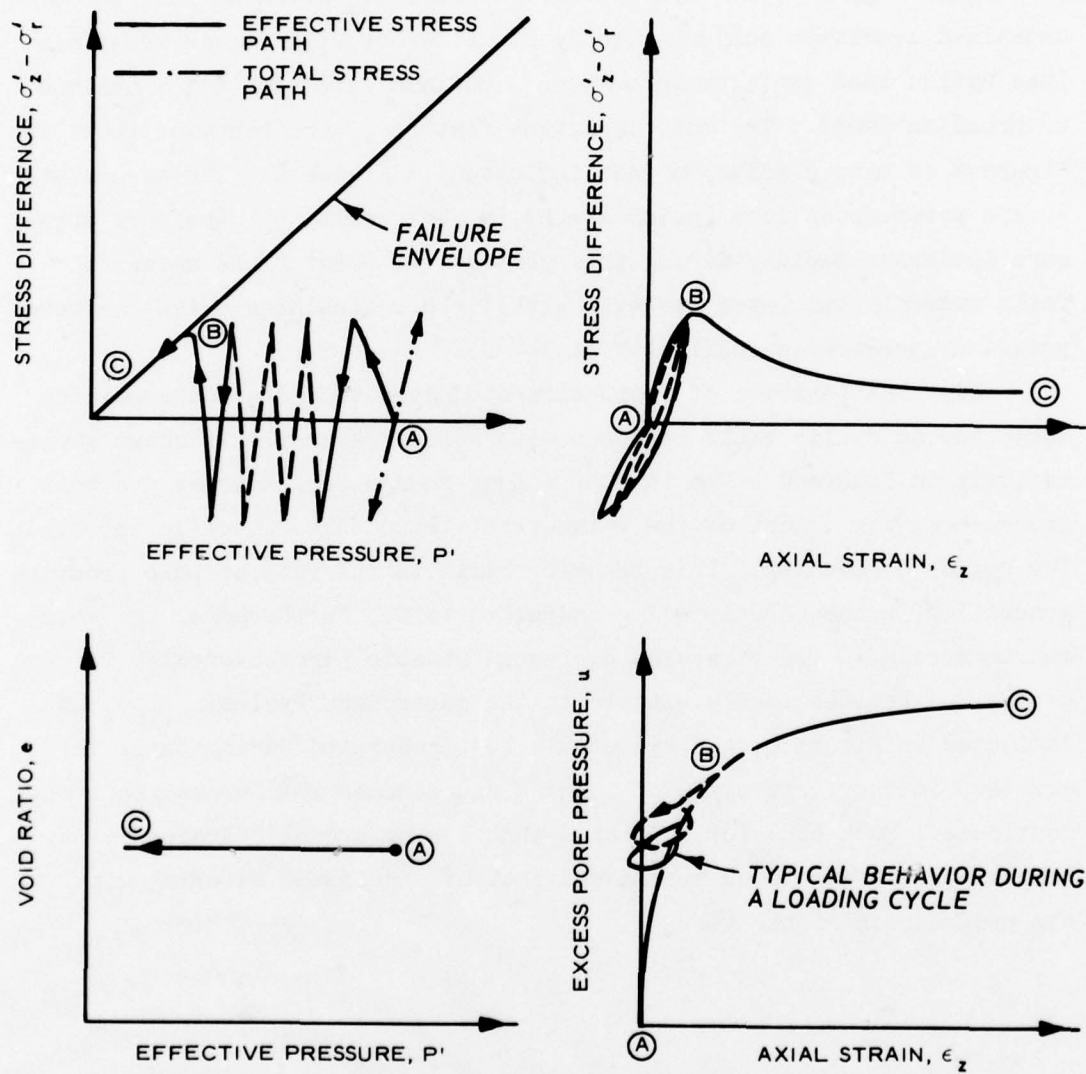


Figure 5. Typical behavior of saturated sand under undrained conditions subjected to cyclic loading with stress reversals in a triaxial test device

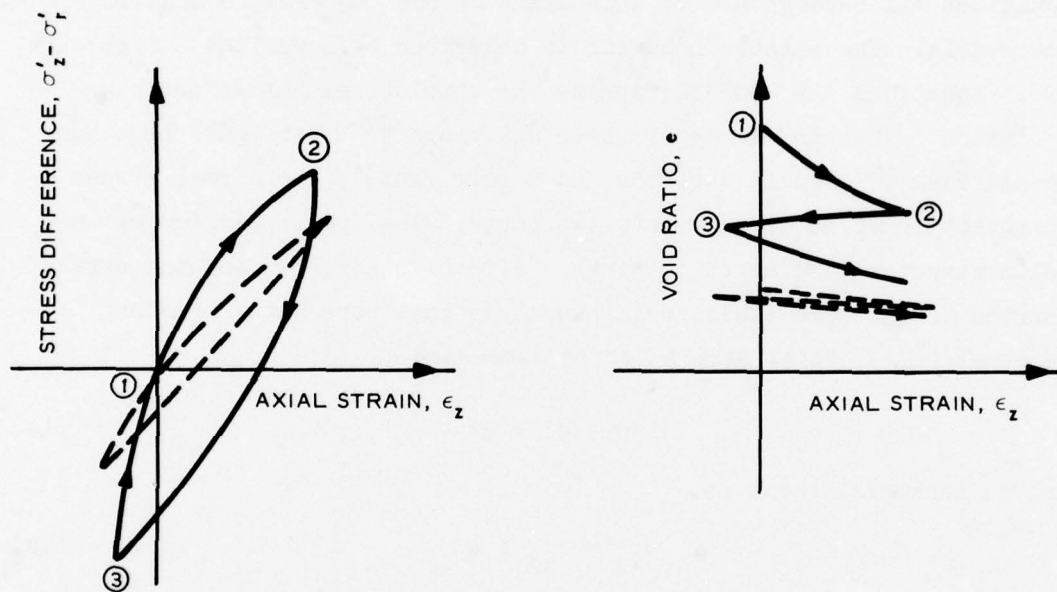


Figure 6. Typical behavior of loose saturated sand under drained conditions subjected to cyclic loading with stress reversals in a triaxial test device

### PART III: FORMULATION OF THE CONSTITUTIVE MODEL

12. The mechanical behavior of saturated cohesionless soils was described qualitatively in Part II. This part presents the development of an elastic-plastic constitutive relationship that describes these various response features.

13. The basic theory of elastic-plastic constitutive models for single-phase (solid) materials is presented in detail in Appendix A. Equations A11 through A16 of Appendix A define the elastic behavior of the models. The plastic behavior is described by Equations A17 through A28. Equations A29 and A30 express the complete elastic-plastic description. In order to apply these equations to a two-phase continuum (consisting of a solid skeleton and a pore fluid), the normal stress components must be divided into two parts: the stress carried by the solid structure, referred to as the "effective stress," and the stress carried by the pore fluid, referred to as the "pore water pressure." Mathematically, total stress can be expressed as

$$\sigma = \sigma' + u \quad (1a)$$

or, in tensorial form, as

$$\sigma_{ij} = \sigma'_{ij} + u\delta_{ij} \quad (1b)$$

where

$\sigma_{ij}$  = total stress tensor

$\sigma'_{ij}$  = effective stress tensor

$u$  = pore pressure

$\delta_{ij}$  = Kronecker delta =  $\begin{cases} 1 & i = j \\ 0 & i \neq j \end{cases}$

For example, in the case of a triaxial test (cylindrical coordinate system  $z$ ,  $r$ , and  $\theta$ ), Equation 1b takes the following form:

$$\begin{cases} \sigma_z = \sigma'_z + u \\ \sigma_r = \sigma_\theta = \sigma'_r + u = \sigma'_\theta + u \end{cases} \quad (2)$$

where  $\sigma_z$  and  $\sigma_r = \sigma_\theta$  are, respectively, the axial and radial total stress components. The following paragraphs contain the mathematical forms of the various response functions developed for the proposed two-phase constitutive relation.

#### Elastic Behavior

14. The behavior of the model in the elastic (recoverable) range is described by the elastic bulk and shear moduli. The elastic bulk modulus is assumed to be a function of effective mean normal stress,\*  $P'$ , or the first invariant of the effective stress tensor  $J'_1$  ( $J'_1 = 3P'$ ) (Figure 7). The elastic shear modulus, on the other hand, is

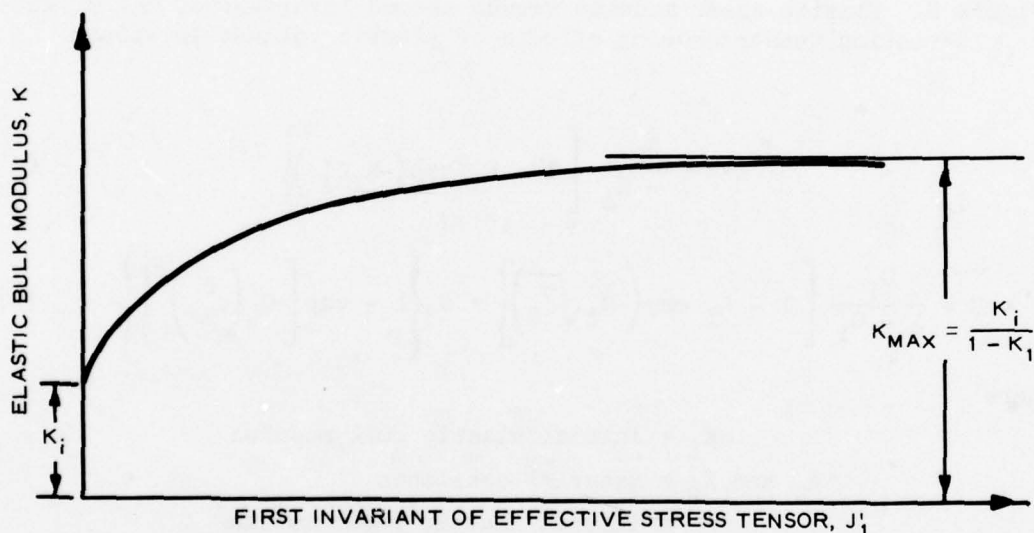


Figure 7. Elastic bulk modulus versus first invariant of the effective stress tensor

assumed to be a function of the second invariant of the stress deviation tensor,  $\bar{J}_2$ , and the plastic volumetric strain,  $\epsilon_{kk}^P$  (Figure 8).\*\*

\* The bulk modulus could also be a function of the plastic volumetric strain.

\*\* The functional forms of the bulk and shear moduli (Equations 3 and 4) could include more terms and provide more flexibility in fitting the behavior of any specific material (cf., Reference 3).



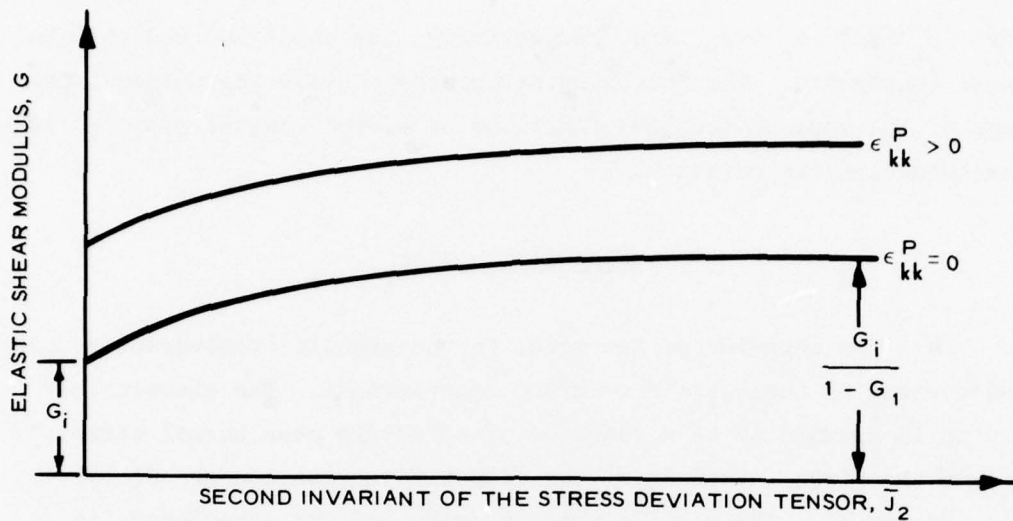


Figure 8. Elastic shear modulus versus second invariant of the stress deviation tensor showing effects of plastic volumetric strain

$$K = \frac{K_i}{1 - K_1} \left[ 1 - K_1 \exp(-K_2 J_1') \right] \quad (3)$$

$$G = \frac{G_i}{1 - G_1} \left[ 1 - G_1 \exp(-G_2 \sqrt{J_2}) \right] + G_3 \left\{ 1 - \exp[-G_4 (\epsilon_{kk}^P)^2] \right\} \quad (4)$$

where

$K_i$  = initial elastic bulk modulus

$K_1$  and  $K_2$  = material constants

$G_i$  = initial elastic shear modulus

$G_1, G_2, G_3$ , and  $G_4$  = material constants

The constants  $K_i$ ,  $K_1$ , and  $K_2$  can be determined from the slope of the unloading curve from an isotropic consolidation test (Figure 9).

The constants  $G_i$ ,  $G_1$ ,  $G_2$ ,  $G_3$ , and  $G_4$  can be determined from the slopes of the unloading stress difference-strain difference curves from drained triaxial tests conducted at different confining pressures (Figure 10).

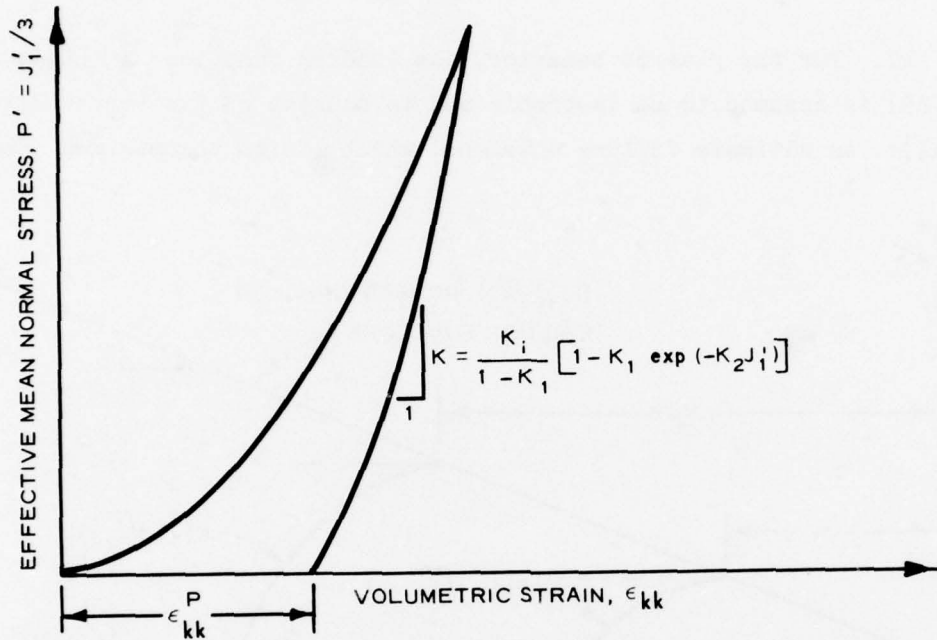


Figure 9. Proposed relationship for isotropic consolidation test

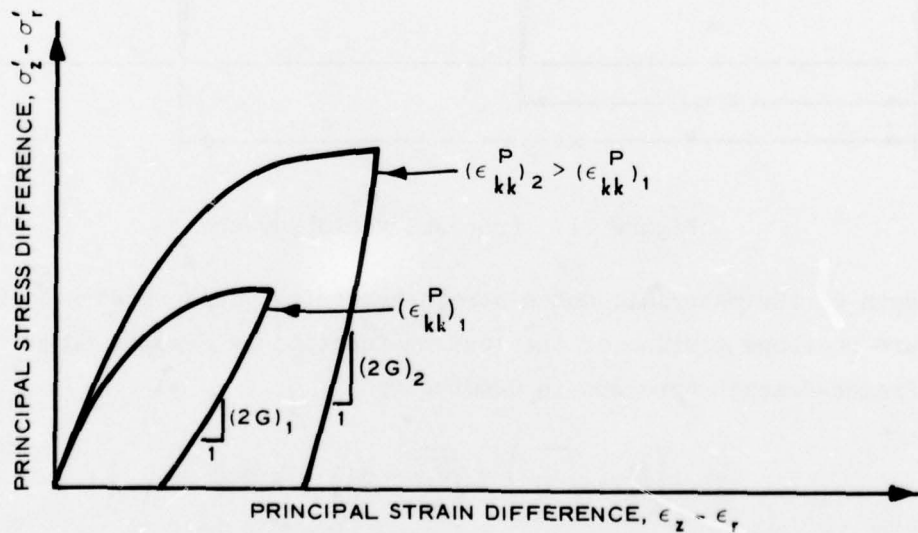


Figure 10. Proposed relationship for triaxial shear test

### Plastic Behavior

15. For the plastic behavior, the loading function  $f$  (Equation A9) is assumed to be isotropic and to consist of two parts (Figure 11): an ultimate failure envelope, which limits the maximum shear

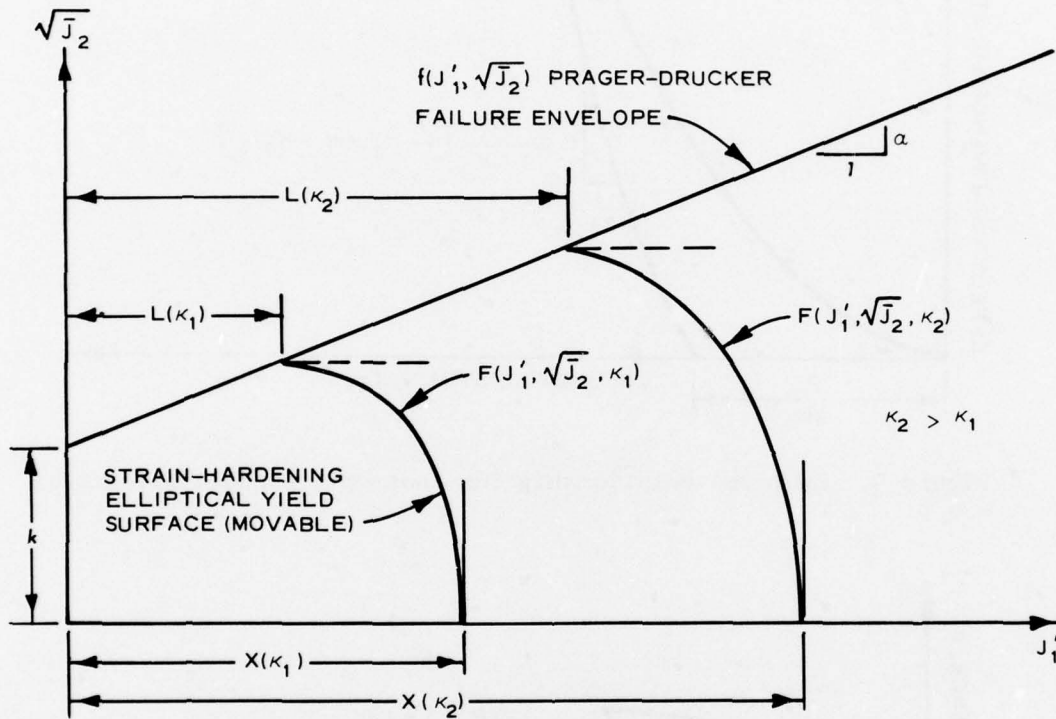


Figure 11. Proposed yield surface

strength of the material, and a strain-hardening yield surface.<sup>3</sup> The failure envelope portion of the loading function is assumed to be of the Prager-Drucker type and is denoted by

$$f(J_1', \sqrt{J_2}) = \sqrt{J_2} - \alpha J_1' - k = 0 \quad (5)$$

and the strain-hardening yield surface is assumed to be elliptical and of the following form:

$$F(J'_1, \sqrt{J_2}, \kappa) = \left[ J'_1 - L(\kappa) \right]^2 + R^2 J_2 - \left[ X(\kappa) - L(\kappa) \right]^2 = 0 \quad (6)$$

where  $k$  and  $\alpha$  are material constants representing the cohesive and frictional strengths of the material, respectively. For cohesionless soil  $k$  is negligible. The parameter  $R$  is the ratio of the major to minor axes of the elliptic yield surface (Figure 11). Note in Figure 11 that  $L(\kappa)$  and  $X(\kappa)$  define the intersections of each hardening surface with the failure envelope  $f(J'_1, \sqrt{J_2})$ , and the  $J'_1$  axis, respectively. The hardening parameter  $\kappa$  is generally a function of the history of plastic volumetric strain. For the present model,  $\kappa$  was chosen as

$$\kappa = \sum_{i=1}^{i=n} \left| \left( d\epsilon_{kk}^P \right)_i \right| \quad (7)$$

where  $\left( d\epsilon_{kk}^P \right)_i$  is the  $i^{th}$  increment of plastic volumetric strain, and  $n$  is the number of increments from the beginning of the loading history. The following relationships were chosen between  $\kappa$ ,  $L(\kappa)$  and  $X(\kappa)$ :

$$L(\kappa) = \begin{cases} \eta(\kappa) & \text{if } \eta(\kappa) > 0 \\ 0 & \text{if } \eta(\kappa) \leq 0 \end{cases} \quad (8)$$

$$X(\kappa) = -\frac{1}{D} \ln \left( 1 - \frac{\kappa}{W} \right) \quad (9)$$

When it is assumed that the failure envelope (Equation 5) intersects each ellipse (Equation 6) at the crown, it follows that

$$\eta(\kappa) = \frac{X(\kappa) - Rk}{1 + \alpha R} = \frac{-\frac{1}{D} \ln \left( 1 - \frac{\kappa}{W} \right) - Rk}{1 + \alpha R} \quad (10)$$



where  $D$  and  $W$  are material constants.  $W$  is the maximum nonrecoverable volumetric compaction that the material can withstand under isotropic consolidation. Because of its impact on the behavior of the model the parameter  $R$  is discussed in the following paragraph.

#### Parameter $R$ and Its Effect on Behavior of Model

16. The value of  $R$  depends on the state of compaction of the material. For contractive material (i.e., loose, Figure 2, curve marked "1  $\rightarrow$  2"), the value of  $R$  is found to be greater than  $1/\alpha$ . For dilative material (i.e., dense, Figure 2 curves marked "1  $\rightarrow$  4" or "1  $\rightarrow$  5"), the value of  $R$  is found to be less than  $1/\alpha$ .  $R = 1/\alpha$  corresponds to the curve marked "1  $\rightarrow$  3" in Figure 2. In this case the strain-hardening yield surface is not allowed to translate relative to the origin of the  $J'_1, \sqrt{J_2}$  axis, and the behavior of the model becomes similar to the critical state model proposed by Schofield and Wroth.<sup>2</sup> These variations in the parameter  $R$  can be accounted for by the following relation:

$$R = \frac{R_i}{1 + R_1} \left\{ 1 + R_1 \exp[-R_2 L(\kappa)] \right\} \quad (11)$$

where  $R_i$ ,  $R_1$ , and  $R_2$  are material constants that can be determined, for example, from  $K_O$  test results (through a trial and error process) so that a good fit to both the stress path and the stress-strain curves is obtained. Equation 11 is used to compute the value of  $R$  whenever the yield surface (Figure 11) is expanding. During unloading in shear, however (i.e. path 2  $\rightarrow$  3 in Figure 12), it is postulated that the yield surface  $ab$  will contract as shown by the dashed curve  $ab'$  in Figure 12. It should be noted that the contraction of the yield surface is not dependent on the plastic strain because, during unloading, plastic strain is constant. The final position of the yield surface is determined by the magnitude of  $\sqrt{J_2}$  at point 3. The value of  $R$  at point 3 is greater than that given by Equation 11 by a factor  $R_f$ .

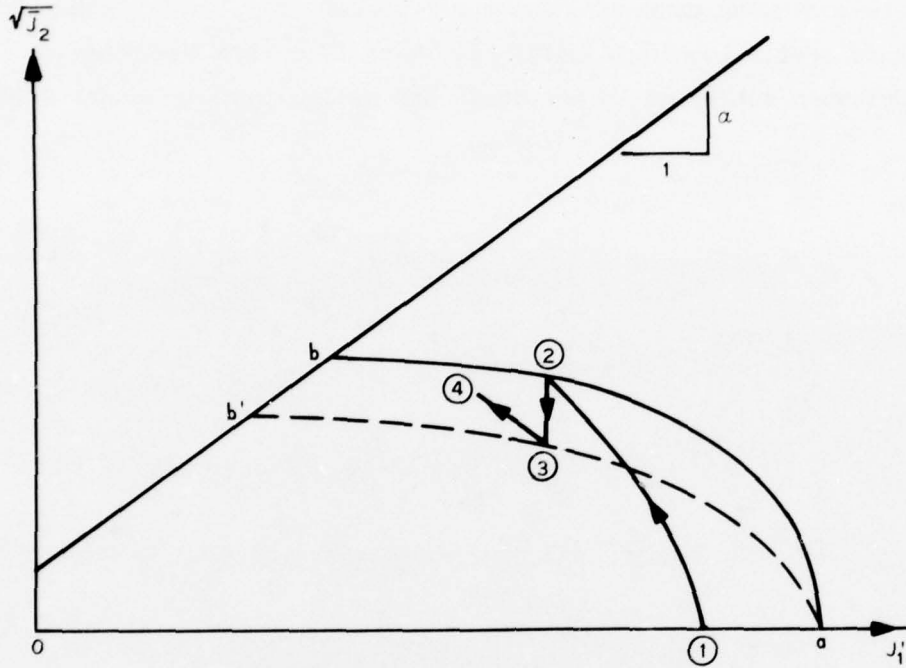


Figure 12. Postulated model behavior during unloading and reloading in shear

Therefore during reloading in shear (path 3  $\rightarrow$  4 in Figure 12) the parameter  $R$  takes the form

$$R = \frac{R_f R_i}{1 + R_1} \left\{ 1 + R_1 \exp[-R_2 L(\kappa)] \right\} \quad (12)$$

where the numerical value of  $R_f$  is determined from the continuity condition at the unload/reload interface at point 3. That is, the value of  $R$  at point 3 is first determined from Equations 6, 8, and 10, where  $X(\kappa)$  corresponding to point a is known and  $L(\kappa)$  corresponds to point b'. This value of  $R$ , together with the values of  $R_i$ ,  $R_1$ , and  $R_2$ , can then be substituted into Equation 12 from which  $R_f$  can be determined.

17. The contraction of the yield surface as discussed in the above paragraph allows considerable flexibility in modeling the behavior

of strain-softening materials and the response of saturated sand under subfailure cyclic loading conditions. Part IV covers the behavior of the model when subjected to monotonic and cyclic loadings under triaxial test.

#### PART IV: BEHAVIOR OF THE MODEL UNDER TRIAXIAL TEST CONDITIONS

18. Current methods of routine stress analysis in geotechnical engineering require material property information, much of which is usually obtained with the triaxial test apparatus. It is of interest, therefore, to investigate the behavior of the proposed model in a triaxial test configuration for both drained and undrained conditions, including cyclic loading. With the adoption of the z-axis of a cylindrical coordinate system (z, r, and  $\theta$ ) as the axis of symmetry of the assumed isotropic specimen, the effective stress tensor  $\sigma'_{ij}$  and the strain tensor  $\epsilon_{ij}$  associated with the triaxial test configuration are

$$\sigma'_{ij} = \begin{bmatrix} \sigma'_z & 0 & 0 \\ 0 & \sigma'_r & 0 \\ 0 & 0 & \sigma'_r \end{bmatrix} \quad (13a)$$

$$\epsilon_{ij} = \begin{bmatrix} \epsilon_z & 0 & 0 \\ 0 & \epsilon_r & 0 \\ 0 & 0 & \epsilon_r \end{bmatrix} \quad (13b)$$

The variables  $J'_1$  (first invariant of the effective stress tensor),  $\bar{J}_2$  (second invariant of the stress deviation tensor), and  $\epsilon_{kk}$  (the volumetric strain  $\Delta V/V$ ) associated with the above stress and strain tensors take the following forms:

$$J'_1 = \sigma'_z + 2\sigma'_r \quad (14a)$$

$$\bar{J}_2 = \frac{1}{3}(\sigma'_z - \sigma'_r)^2 \quad (14b)$$



$$\epsilon_{kk} = \epsilon_z + 2\epsilon_r = \frac{\Delta V}{V} \quad (14c)$$

Triaxial tests on saturated sands generally are performed in two phases: (a) an isotropic consolidation phase and (b) a shear phase. The shear phase may be performed either drained or undrained. These phases are discussed below.

#### Isotropic Consolidation Phase

19. During the isotropic consolidation phase of the triaxial test,

$$\sigma'_z = \sigma'_r = \frac{J'_1}{3} \quad (15a)$$

$$\epsilon_z = \epsilon_r = \frac{\epsilon_{kk}}{3} \quad (15b)$$

The relation between the elastic volumetric strain increment and the increment of the first invariant of the effective stress tensor is (see Equation A12)

$$dJ'_1 = 3K d\epsilon_{kk}^E \quad (16)$$

where the elastic bulk modulus  $K$  is given by Equation 3. Substitution of Equation 3 into Equation 16 and integration of the resulting expression provides the following relation between the elastic volumetric strain  $\epsilon_{kk}^E$  and  $J'_1$ :

$$\epsilon_{kk}^E = \frac{1 - K_1}{3K_2 K_1} \ln \left[ \frac{\exp(K_2 J'_1) - K_1}{1 - K_1} \right] \quad (17)$$

The relation between the plastic volumetric strain  $\epsilon_{kk}^P$  and  $J'_1$  is given by Equation 9, where  $\kappa$  (Equation 7) for this phase of the test is  $\epsilon_{kk}^P$  and  $X(\kappa)$  is  $J'_1$ , thus

$$\epsilon_{kk}^P = W \left[ 1 - \exp(-DJ_1') \right] \quad (18)$$

As a result of Equations 17 and 18, the total volumetric strain takes the following form:

$$\epsilon_{kk} = \frac{1 - K_1}{3K_2K_i} \ln \left[ \frac{\exp(K_2J_1') - K_1}{1 - K_1} \right] + W \left[ 1 - \exp(-DJ_1') \right] \quad (19)$$

Equations 17 through 19 provide a complete specification for the behavior of the material during the isotropic consolidation phase of the triaxial test.

20. The qualitative behavior of the model during isotropic consolidation is shown in Figure 13. The slope of the  $J_1'$  versus  $\epsilon_{kk}$  curve during initial loading can be obtained from Equation 19:

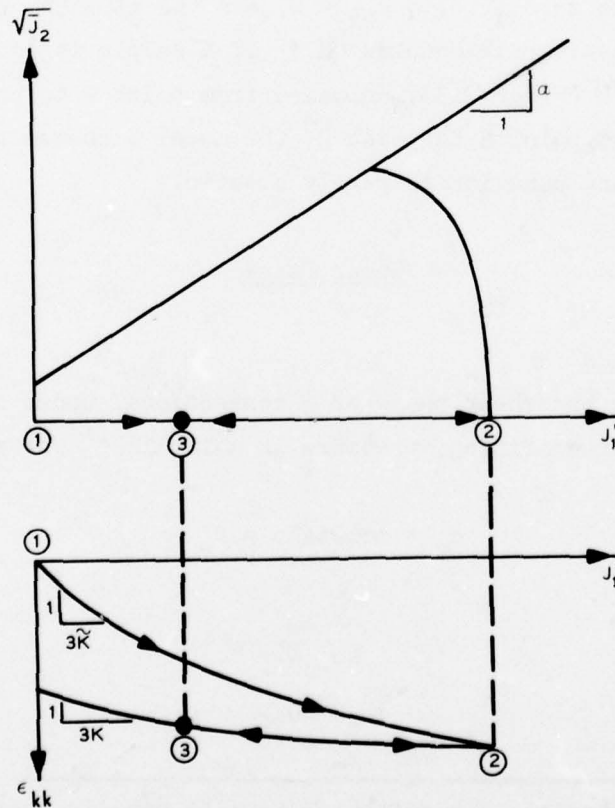


Figure 13. Behavior of the model under cyclic isotropic consolidation

$$\frac{dJ'_1}{d\epsilon_{kk}} = \frac{1}{\frac{3K_i}{1 - K_1} \left[ 1 - K_1 \exp(-K_2 J'_1) \right] + WD \exp(-DJ'_1)} = 3\tilde{K} \quad (20)$$

where  $\tilde{K}$  is the apparent bulk modulus of the material. The combination of Equations 3, 18, and 20 results in

$$\tilde{K} = \frac{1}{\frac{1}{K} + 3D \left( W - \epsilon_{kk}^P \right)} \quad (21)$$

The second term in the denominator of Equation 21 represents a softening term; i.e., it accounts for the fact that  $\tilde{K}$  is initially softer than the elastic bulk modulus  $K$ . At higher pressures, however, this softening term becomes zero (i.e.,  $\epsilon_{kk}^P = W$ ) and the apparent bulk modulus  $\tilde{K}$  equals the elastic bulk modulus  $K$ .<sup>\*</sup> If a sample is consolidated from point 1 to point 2 (Figure 13), unloaded from point 2 to point 3, and then reloaded from point 3 to point 2, the model dictates that the unloading-reloading behavior is purely elastic.

#### Shear Phase

##### Undrained condition

21. During the shear phase of a conventional undrained triaxial test, the cell, or confining, pressure is maintained constant: i.e.,

$$\sigma_r = \text{constant} = P'_c \quad (22a)$$

hence,

$$d\sigma_r = 0 \quad (22b)$$

---

\* For a dense material, the softening term is usually small, and the modulus  $\tilde{K}$  closely approximates the elastic bulk modulus.

where  $P'_c$  is the confining pressure at the end of the isotropic consolidation phase. The stipulation that the shear phase is performed undrained means that the volumetric strain is constant and equal to the volumetric strain achieved at the end of the consolidation phase.\* Accordingly, for an undrained shear phase,

$$d\epsilon_{kk} = d\epsilon_{kk}^E + d\epsilon_{kk}^P = 0 \quad (23a)$$

which leads to

$$d\epsilon_r = -\frac{1}{2} d\epsilon_z \quad (23b)$$

The shear phase up to failure (Equation 5) can be accomplished by either monotonic or cyclic loading. At failure, the shear strength of the material can either (a) increase (i.e., undergo strain hardening), (b) decrease (i.e., undergo strain softening), or (c) remain constant (e.g., if the material is at its critical density, Figure 2, point 3). The behavior of the model under these three conditions is examined separately below.

22. Prefailure response under monotonic loading. The total volumetric strain at the end of the consolidation phase of the test can be obtained from Equations 9 and 17:

$$\epsilon_{kk} = \frac{1 - K_1}{3K_2K_i} \ln \left[ \frac{\exp(K_2J'_1) - K_1}{1 - K_1} \right] + W \left\{ 1 - \exp[-DX(\kappa)] \right\} \quad (24a)$$

or

$$\epsilon_{kk} = \frac{1 - K_1}{3K_2K_i} \ln \left[ \frac{\exp(3K_2P'_c) - K_1}{1 - K_1} \right] + W \left[ 1 - \exp(-3DP'_c) \right] \quad (24b)$$

---

\* Undrained shear actually means no change in water content; the condition of constant volumetric strain is only an approximation.



The equation of the hardening surface (Equation 6) for the triaxial configuration takes the following form:

$$\left[J_1' - L(\kappa)\right]^2 + \frac{R^2}{3} (\sigma_z' - \sigma_r')^2 - \left[X(\kappa) - L(\kappa)\right]^2 = 0 \quad (25)$$

An expression for the effective stress path in the shear phase (i.e.,  $\sigma_z' - \sigma_r'$  versus  $J_1'$ ) can be obtained by the combination of Equations 10, 24b, and 25:

$$\begin{aligned} & \left( J_1' (1 + \alpha R) + Rk + \frac{1}{D} \ln \left\{ 1 + \frac{1 - K_1}{3WK_2K_i} \ln \left[ \frac{\exp(K_2J_1') - K_1}{\exp(3K_2P_c') - K_1} \right] \right. \right. \\ & \quad \left. \left. - \left[ 1 - \exp(-3DP_c') \right] \right\} \right)^2 - \\ & \left( Rk - \frac{\alpha R}{D} \ln \left\{ 1 + \frac{1 - K_1}{3WK_2K_i} \ln \left[ \frac{\exp(K_2J_1') - K_1}{\exp(3K_2P_c') - K_1} \right] - \left[ 1 - \exp(-3DP_c') \right] \right\} \right)^2 \\ & + \frac{R^2}{3} (1 + \alpha R)^2 (\sigma_z' - \sigma_r')^2 = 0 \end{aligned} \quad (26)$$

Figure 14 shows a typical effective stress path produced by Equation 26. The sample is isotropically consolidated from point 1 to point 2. The path indicated by point 2 → 3 represents the prefailure effective stress path under monotonic loading. The total stress path is indicated by point 2 → 4. Since the effective and the total stress paths are known, the excess pore pressure  $u$  can easily be determined as indicated in Figure 14. Because the pore pressure and the effective stress tensor have been determined, the complete strain tensor can be obtained from Equation A29 by use of Equations 3, 4, 9, 10, and 25 (with  $R$  calculated from Equation 11). A computer program called TDRIVER was developed to solve numerically this system of equations, as well as Equation A29, and to generate various plots of stress-strain and pore

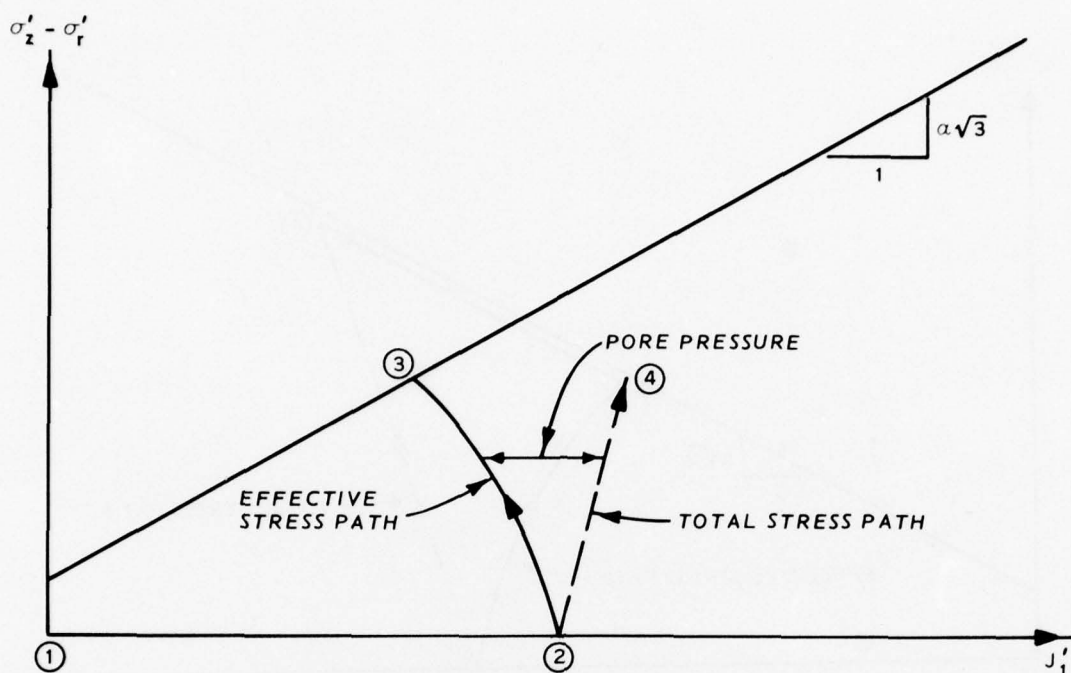


Figure 14. Typical effective stress path produced by Equation 26

pressure response for undrained triaxial conditions. This program and its flow charts are available upon request.

23. Postfailure response of dilative materials. Figure 15 represents a typical triaxial test stress path for dilative material. The plastic volumetric strain increment along the path 3 → 4 can be obtained from Equations 5, A20, and A28 as

$$d\epsilon_{kk}^P = -3 \left[ \frac{df(J'_1, \sqrt{J'_2})}{9K\alpha^2 + G} \right] \alpha \quad (27)$$

Since the total volumetric strain increment during the shear phase is assumed to be zero, the elastic volumetric strain increment can be set equal to the negative of the plastic volumetric strain increment; that is

$$d\epsilon_{kk}^E = 3 \left[ \frac{df(J'_1, \sqrt{J'_2})}{9K\alpha^2 + G} \right] \alpha \quad (28)$$

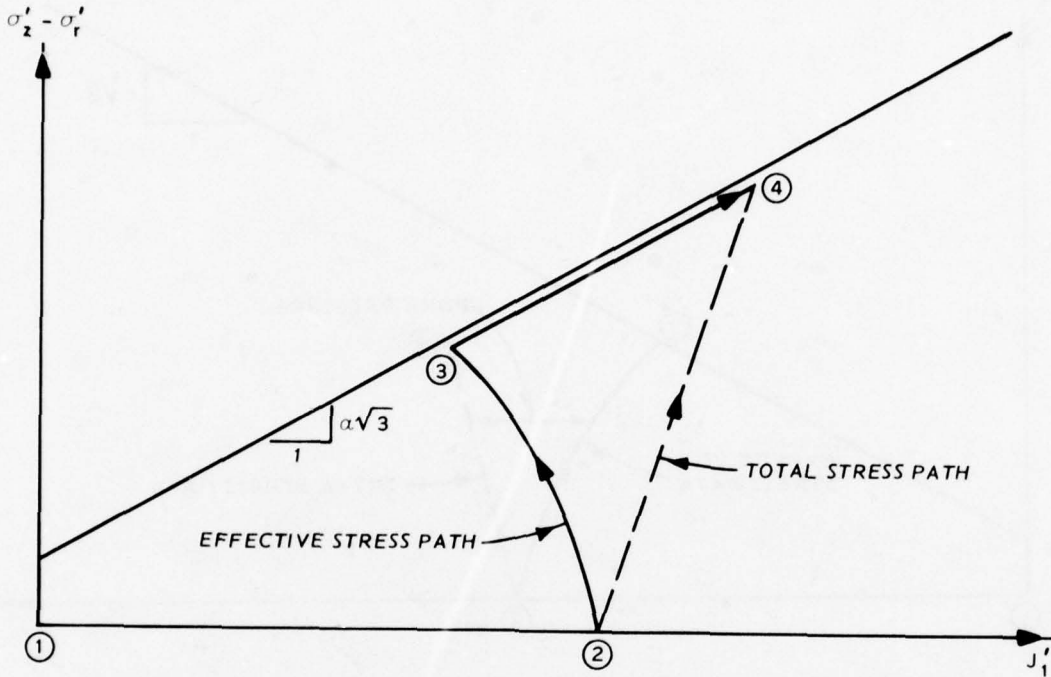


Figure 15. Typical stress path for dilative material under undrained shear (triaxial test) conditions

The hardening parameter  $\kappa$  along the path 3  $\rightarrow$  4 (see Figure 15) is

$$\kappa = \left( \left| \epsilon_{kk}^P \right| \right)_{1-2} + \left( \left| \epsilon_{kk}^P \right| \right)_{2-3} + \left( \left| \epsilon_{kk}^P \right| \right)_{3-4} \quad (29)$$

The intersection of the strain-hardening yield surface, Equation 6, with the  $J'_1$  axis can be obtained from Equation 9. The intersection of the yield surface with the failure envelope is given by

$$L(\kappa) = \min \left[ J'_1, X(\kappa) \right] \quad (30)$$

The value of  $R$  can be determined from

$$R(\kappa) = \frac{X(\kappa) - L(\kappa)}{k + \alpha L(\kappa)} \quad (31)$$

Note that when  $R = 0$  (i.e.,  $X(\kappa) = L(\kappa)$ ), the material reaches its peak shear strength (point 4, Figure 15).

24. In summary, for a dilative material,  $R$  is a function of  $\kappa$  through Equation 11, and  $\kappa$  is equal to the actual plastic volumetric strain along the paths  $1 \rightarrow 2$  and  $2 \rightarrow 3$  in Figure 15. Along the path  $3 \rightarrow 4$ , however,  $\kappa$  is given by Equation 29, and  $R$  is a function of  $\kappa$  through Equation 31. Equation A29 will give the total strain when the computer program TDRIVER is used.

25. Postfailure response of contractive material. Figure 2 (curve  $1 \rightarrow 2$ ) shows the typical behavior of a contractive material under the undrained triaxial test condition. Figure 16 represents the model simulation of this behavior. The treatment of path  $1 \rightarrow 2 \rightarrow 3$  is similar to the prefailure behavior discussed in the previous paragraph. Beyond point 3 the material strain softens. This may be viewed as a release of elastic strain with a concomitant buildup of plastic strain. The path  $3 \rightarrow b$ , therefore, can be simulated by the model in two steps: elastic unloading from point 3 to point a followed by elastic-plastic loading from point a to point b.

26. Since path  $3 \rightarrow a$  is purely elastic,

$$d\epsilon_{kk} = d\epsilon_{kk}^E = d\epsilon_{kk}^P = 0 \quad (32)$$

Therefore,  $\kappa$  and  $X(\kappa)$  remain constants and the yield surface (Equation 6) is inactive along this path. The value of  $L$ , however, is variable and can be computed from Equations 6 and 10. The long-dashed line shown in the left sketch of Figure 16 represents the position of the yield surface at point a. The value of  $R$  corresponding to this yield surface is computed from Equation 12. Along the path  $a \rightarrow b$ , the total volumetric strain, which is constant, can be obtained from Equation 24a. The effective stress path  $a \rightarrow b$  can be determined from Equation 26, and the computer program TDRIVER may be used to compute total strain along the path  $3 \rightarrow a \rightarrow b$ .

27. The above process is repeated along the path  $b \rightarrow 4$  as shown by the short-dashed line in Figure 16. Note that the loading increment



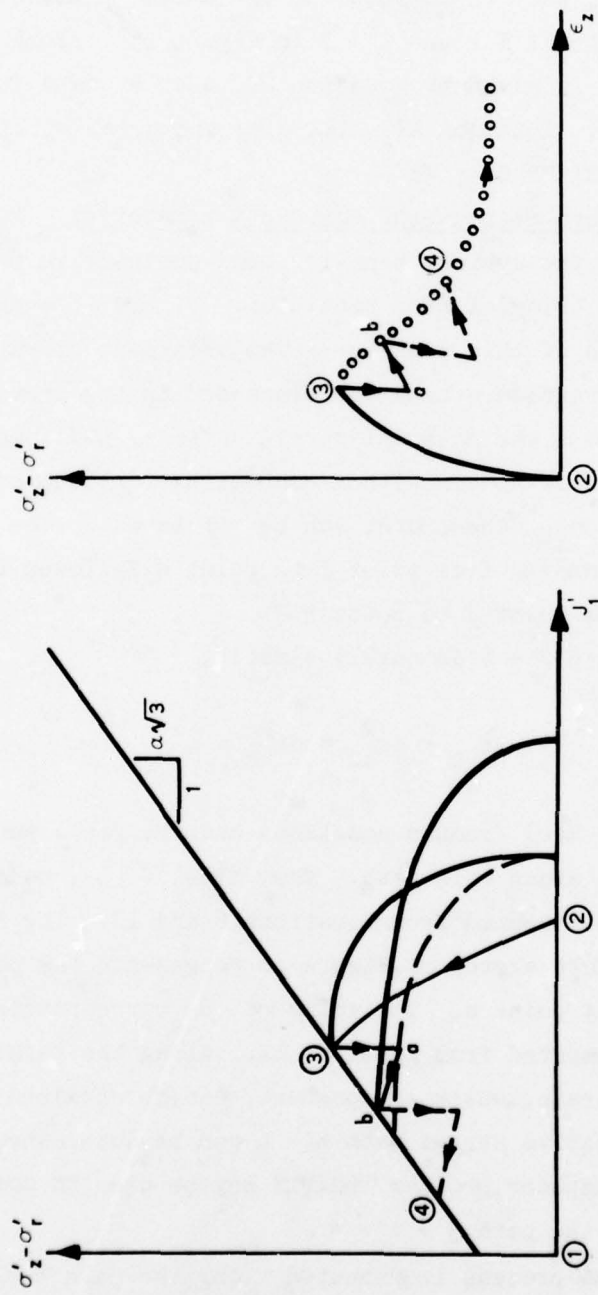


Figure 16. Model simulation of strain-softening material under undrained shear (triaxial test) conditions

between 3  $\rightarrow$  4 can be divided into  $n$  increments so that the dotted portion of the stress-strain curve shown in Figure 16 can be closely adhered to.

28. Prefailure response under undrained cyclic loading. Figures 4 and 5 show the typical behavior of saturated soil under undrained cyclic shear loading. This behavior can be simulated by the model similarly to the manner described for the treatment of strain-softening materials. The path 3  $\rightarrow$  a (Figure 17) is purely elastic, in which  $\kappa$  and  $X(\kappa)$  are constant while  $L$  is variable. From a to b the path is elastic-plastic for which the total strain tensor can be obtained from Equation A29 with the use of the computer program TDRIVER.

#### Drained condition

29. For the case of a drained shear test the effective stresses are identical to the total stresses and the stress path is known a priori. Hence, the model treats this case identically to the undrained case except that the restriction of no volume change during the shear phase is dropped. The material response is determined directly from Equation A29 using the computer program TDRIVER.

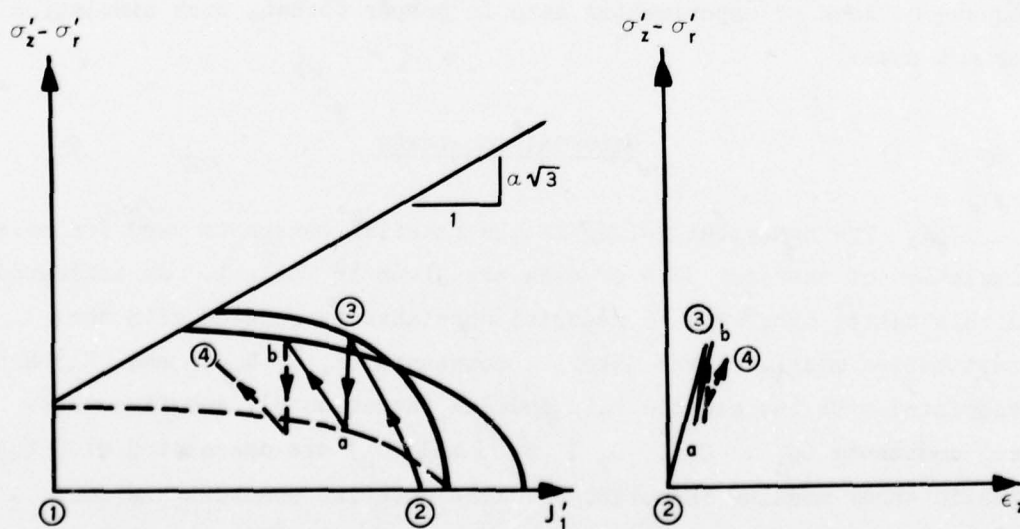


Figure 17. Model simulation of undrained cyclic shear loading conditions

## PART V: COMPARISON OF LABORATORY TEST DATA WITH MODEL PREDICTION

30. In order to demonstrate the versatility of the proposed constitutive model for simulation of the wide variety stress-strain-pore pressure responses observed in tests of saturated cohesionless soils (as seen in Figures 2 and 4), four sets of experimental data were considered. The first set of data (data set 1) typifies the behavior of contractive (loose) materials. As indicated in Figure 2 (curves 1  $\rightarrow$  3), this type of material exhibits an increase in pore pressure during undrained shear. The second set of data (data set 2) typifies the behavior of dilative (dense) materials. During undrained shear these materials exhibit an increase in effective pressure and a consequent decrease in pore pressure (curves 1  $\rightarrow$  5, Figure 2). The third set of data (data set 3) typifies the behavior of very loose (work-softening) materials subjected to undrained shear (curves 1  $\rightarrow$  2, Figure 2). The fourth set of data (data set 4) demonstrates the behavior of loose saturated sand under undrained cyclic shear loading. As shown in Figure 4, undrained cyclic shear causes a rapid decrease in effective pressure and a consequent increase in pore pressure. The model can also simulate the response of dense saturated sand under undrained cyclic shear loading. However, because of lack of experimental data in proper format, such simulation was not made.

### Material Constants

31. The numerical values of the material constants used for model simulation of the four sets of data are given in Table 1. As indicated in this table, there are 15 material constants associated with the constitutive model. Three material constants ( $K_1$ ,  $K_1$ , and  $K_2$ ) are associated with the elastic bulk modulus (Equation 3), and five material constants ( $G_1$ ,  $G_1$ ,  $G_2$ ,  $G_3$ , and  $G_4$ ) are associated with the elastic shear modulus (Equation 4). The material constants  $k$  and  $\alpha$  relate to the ultimate failure envelope of the material (Equation 5), and the material constants  $W$  and  $D$  are associated with the hardening

function (Equation 9). The material constants  $R_i$ ,  $R_1$ , and  $R_2$  are associated with the parameter  $R$  (Equation 11), which defines the ratio of the major to the minor axes of the elliptic yield surface. Direct determination of these material constants requires an elaborate set of experimental data. Because of the lack of detailed experimental data some of the material constants in Table 1 were assumed to be zero. In addition, the numerical values of some of the other constants had to be determined by trial and error, by the use of the computer program TDRIVER in order to obtain a good fit to the available experimental data, in lieu of the values being determined directly from test results. Accordingly, the entire capability of the constitutive model was not utilized in simulating these experimental data. The following sections compare the model predictions with these experimental data.

#### Comparison with Contractive Material (Data Set 1)

32. The experimental data for the contractive material (Reid-Bedford Model sand) were obtained from Reference 4. The data consist of results from one load/unload isotropic consolidation test and two consolidated undrained triaxial tests. The tests were conducted on saturated samples of Reid-Bedford Model sand having an initial relative density of approximately 20 percent. Figures 18 through 21 compare the actual test results with predicted behavior by the model for this set of data. The result of the consolidation test is shown in Figure 18. Figure 19 shows effective stress paths in principal stress difference-effective mean normal stress space. The shear stress-strain relations, in terms of principal stress difference versus axial strain, are shown in Figure 20. Figure 21 shows excess pore pressures versus axial strain. Figures 18 through 21 indicate that the constitutive model qualitatively simulates the response of contractive materials.

#### Comparison with Dilative Material (Data Set 2)

33. Experimental data for a dilative material were obtained from



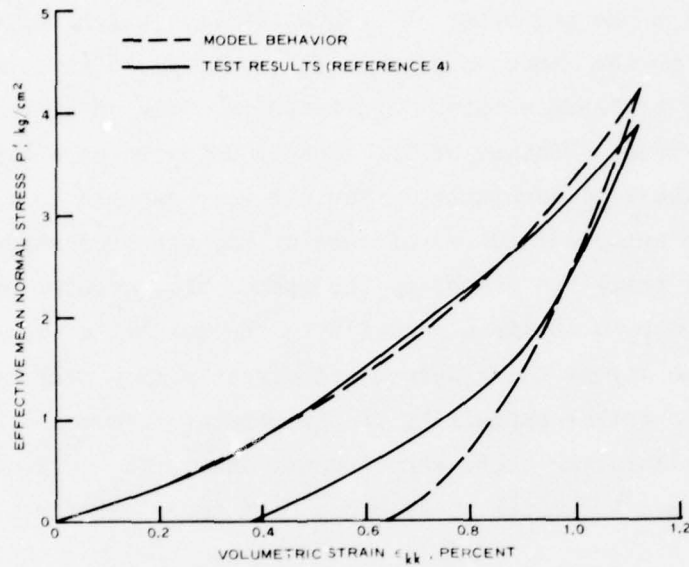


Figure 18. Isotropic consolidation response; experimental versus model; data set 1

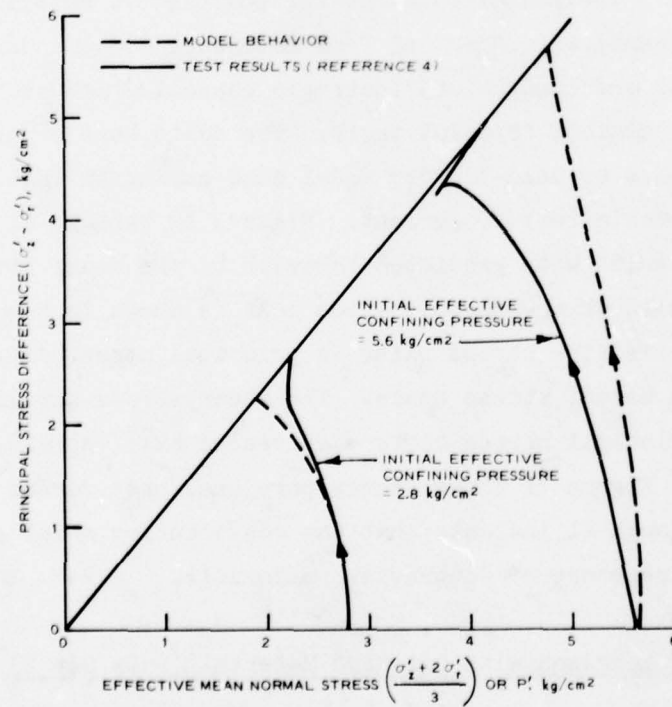


Figure 19. Comparison of effective stress paths for consolidated undrained triaxial tests; experimental versus model; data set 1

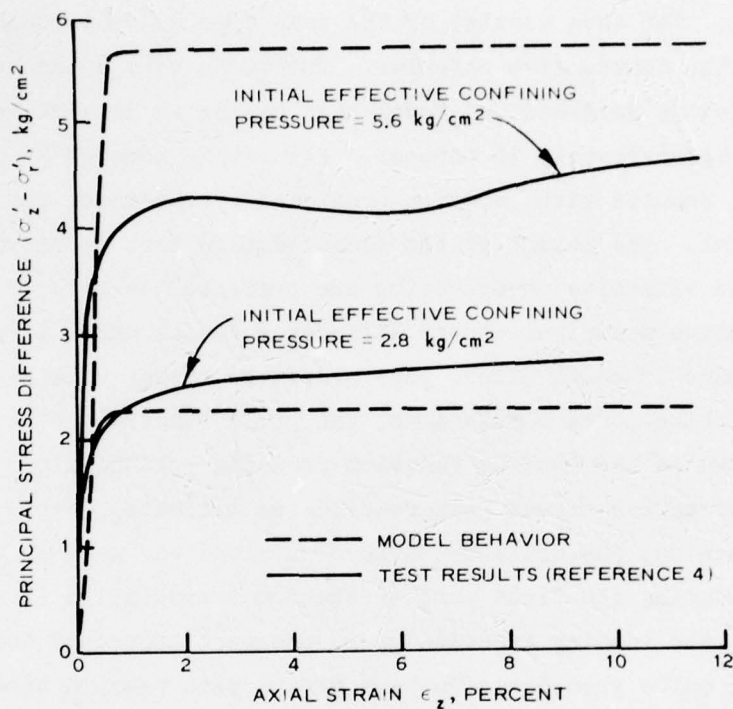


Figure 20. Stress difference versus axial strain response for undrained triaxial tests; experimental model; data set 1

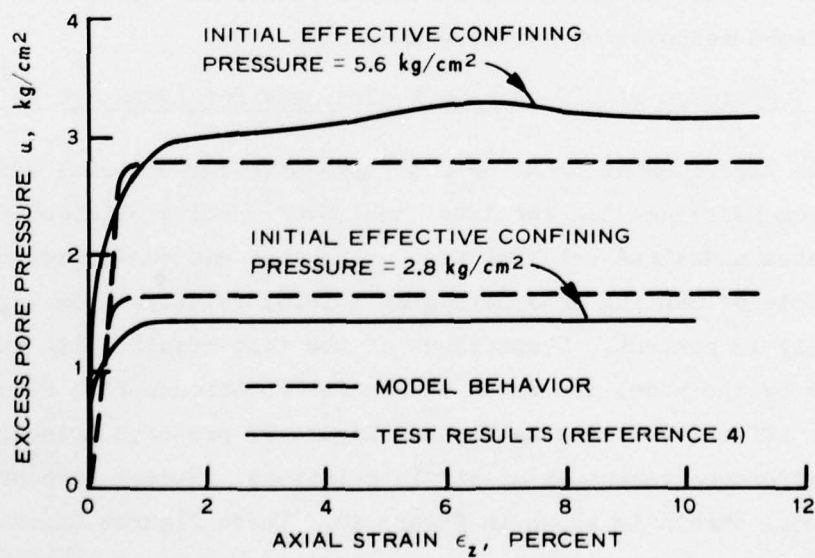


Figure 21. Excess pore water pressure versus axial strain response from undrained triaxial tests; experimental versus model; data set 1

Reference 1. The data consist of the same type of test results as reported for the contractive material. The tests were conducted on saturated samples of Reid-Bedford Model sand having an initial relative density of approximately 76 percent. Figures 22 through 25 compare the actual test results with behavior predicted by the model for the dilative material. The result of the consolidation test is shown in Figure 22. The effective stress paths are presented in Figure 23, and Figure 24 shows principal stress difference versus axial strain relations. Figure 25 shows excess pore pressures versus axial strain. In generating these model simulations, the yield function  $F$  (the elliptic cap) was used as the loading function from the beginning of the test until the effective stress path reached the ultimate failure envelope  $f$ ; from then on, the ultimate failure envelope was used as the loading function. During the first part of the model simulation (i.e., when  $F$  was used as the loading function) pore pressure increased and reached its maximum value when the effective stress path reached the ultimate failure envelope. As the test continued, excess pore pressure then decreased and eventually became negative. The experimental/model comparisons shown in Figures 22 through 25 indicate that the proposed constitutive relation can qualitatively simulate the stress-strain-pore pressure response of dilative materials.

#### Comparison with Strain-Softening Behavior (Data Set 3)

34. Experimental data for a strain-softening material were obtained from Reference 5. The data consist of results obtained from one consolidated undrained triaxial test. The test was conducted on a saturated sample of Banding sand having an initial relative density of approximately 13 percent. Comparisons of the test results with behavior predicted by the model are shown in Figures 26 through 28. Figure 26 shows the effective stress paths, and Figure 27 presents principal stress difference versus axial strain relations. Excess pore pressure versus axial strain is shown in Figure 28. These figures illustrate that the proposed constitutive relation quite capably simulates the stress-strain-pore pressure response of work-softening materials.

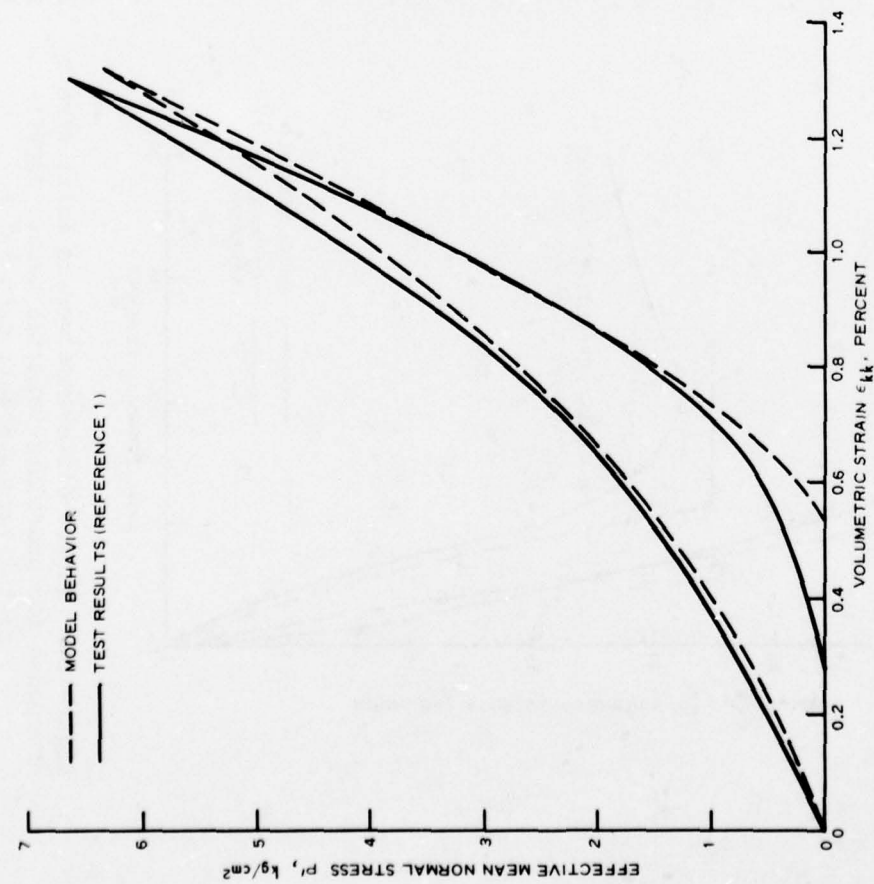


Figure 22. Isotropic consolidation response; experimental versus model; data set 2

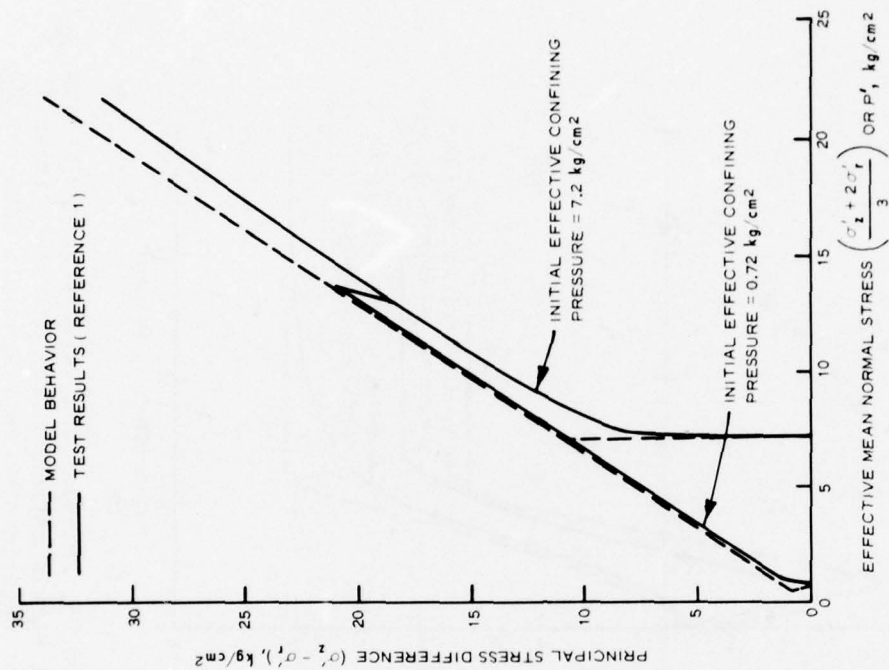


Figure 23. Comparison of effective stress paths for consolidated undrained triaxial tests; experimental versus model; data set 2



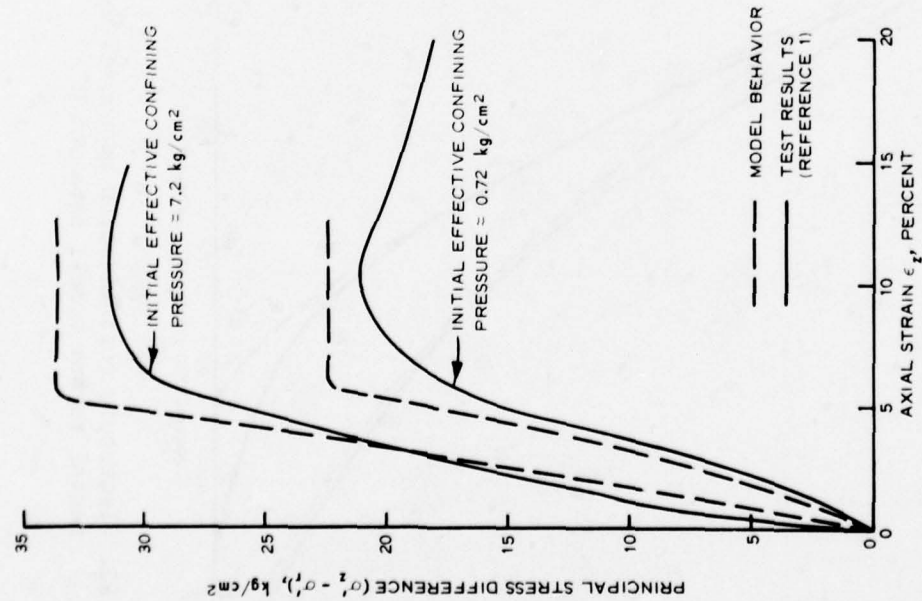


Figure 24. Stress difference versus axial strain response for undrained triaxial tests; experimental versus model; data set 2

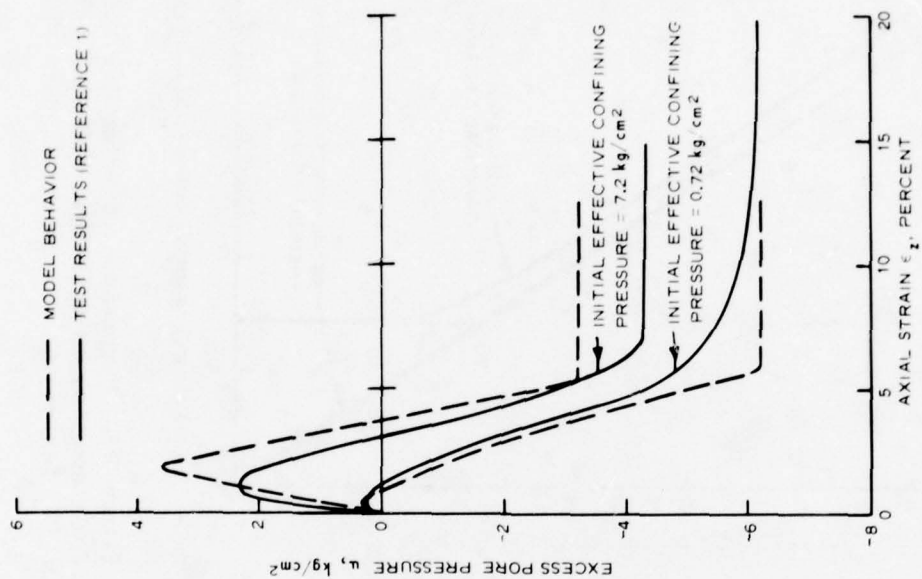


Figure 25. Excess pore water pressure versus axial strain response from undrained triaxial tests; experimental versus model; data set 2

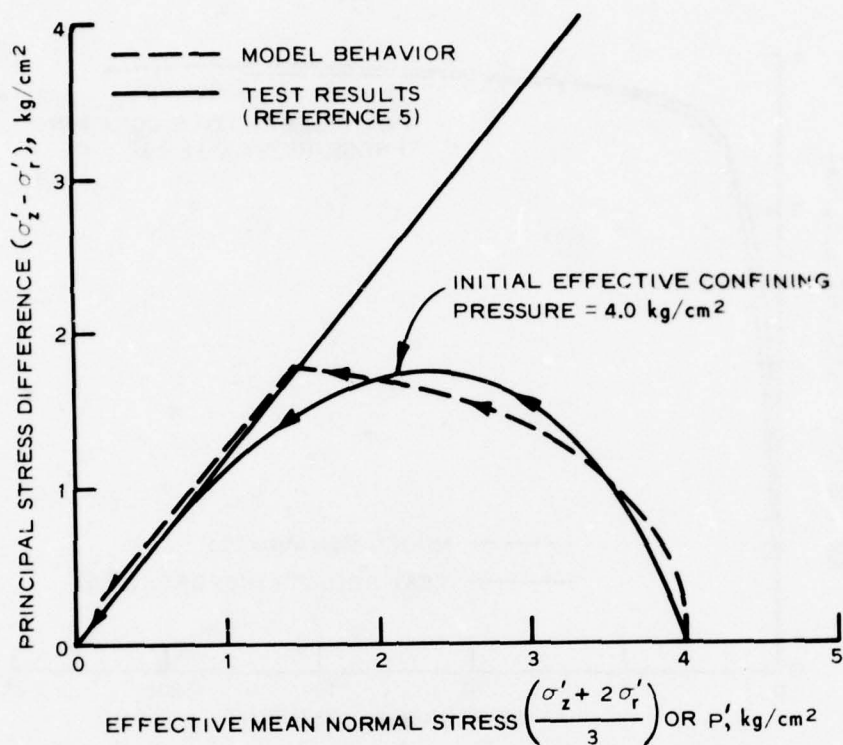


Figure 26. Effective stress paths for consolidated undrained triaxial tests; experimental versus model; data set 3

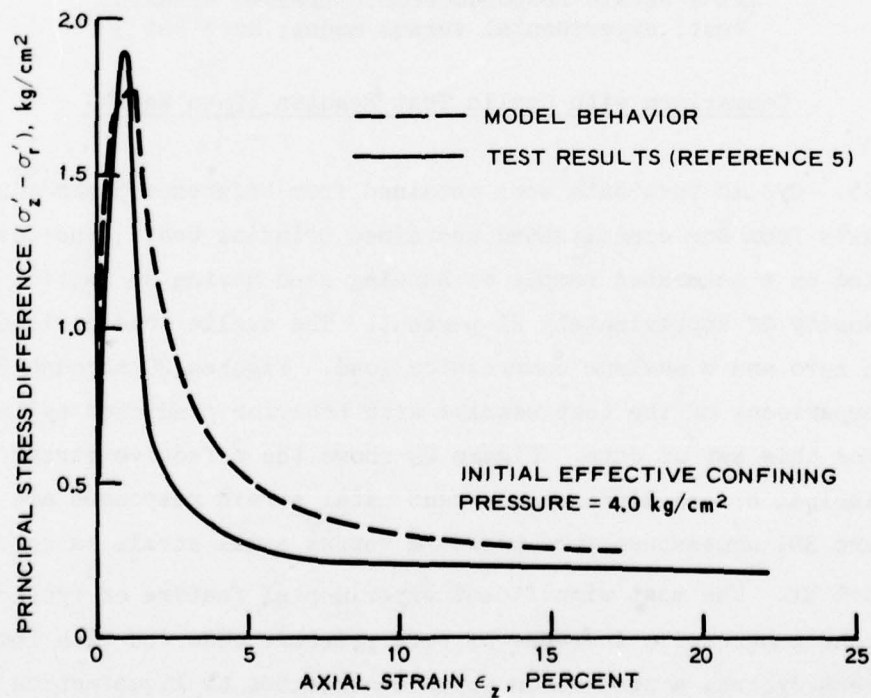


Figure 27. Principal stress difference versus axial strain response from undrained triaxial test; experimental versus model; data set 3

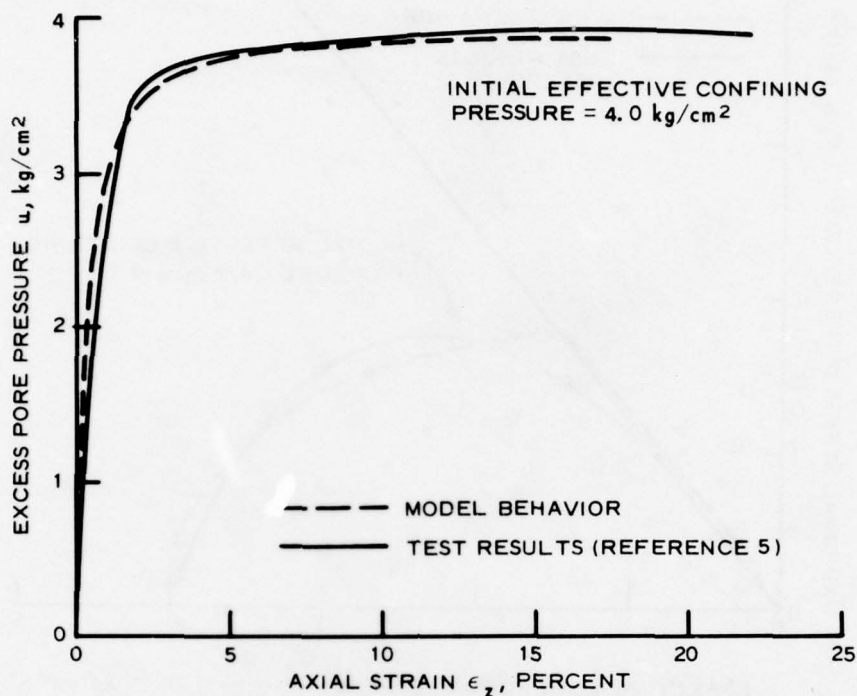


Figure 28. Excess pore water pressure versus axial strain response from undrained triaxial test; experimental versus model; data set 3

Comparison with Cyclic Test Results (Data Set 4)

35. Cyclic test data were obtained from Reference 5 and consist of results from one consolidated undrained triaxial test. The test was conducted on a saturated sample of Banding sand having an initial relative density of approximately 21 percent. The cyclic load oscillated between zero and a maximum compression load. Figures 29 through 31 show comparisons of the test results with behavior predicted by the model for this set of data. Figure 29 shows the effective stress paths. The principal stress difference versus axial strain responses are shown in Figure 30, and excess pore pressure versus axial strain is compared in Figure 31. The most significant experimental feature of cyclic loading is the progressive increase of pore pressure observed with increasing stress cycles, a phenomenon which contributes to liquefaction of

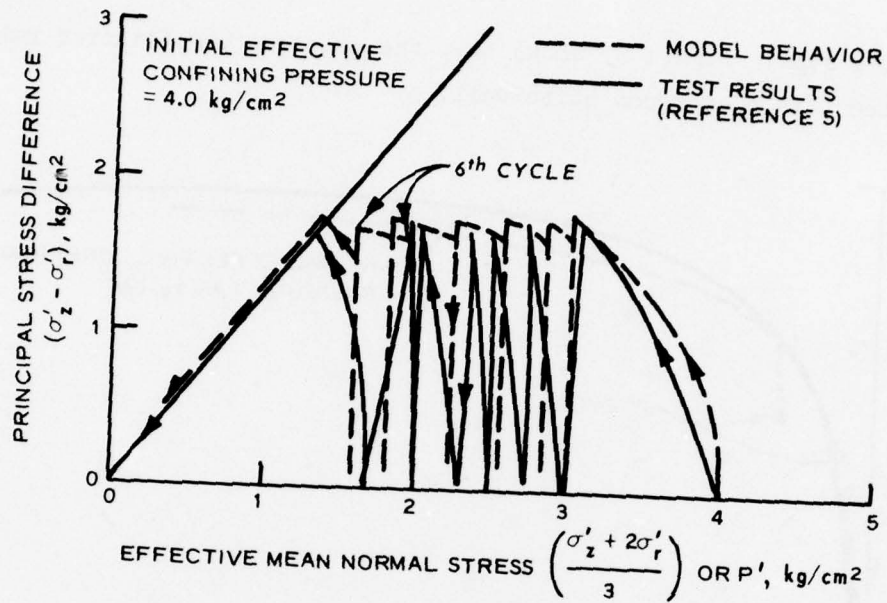


Figure 29. Effective stress paths for consolidated undrained (cyclic shear) triaxial test; experimental versus model; data set 4

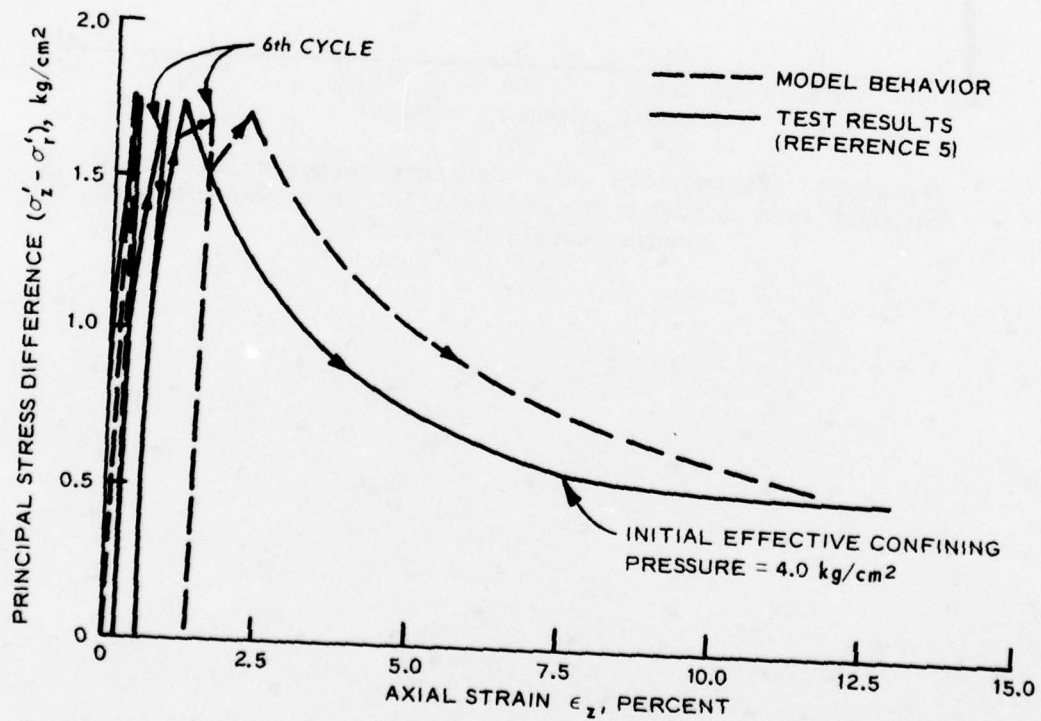


Figure 30. Principal stress difference versus axial strain response from cycled undrained triaxial test; experimental versus model; data set 4



saturated sand. Figure 31 shows that the proposed constitutive relation simulates this phenomenon quite well.

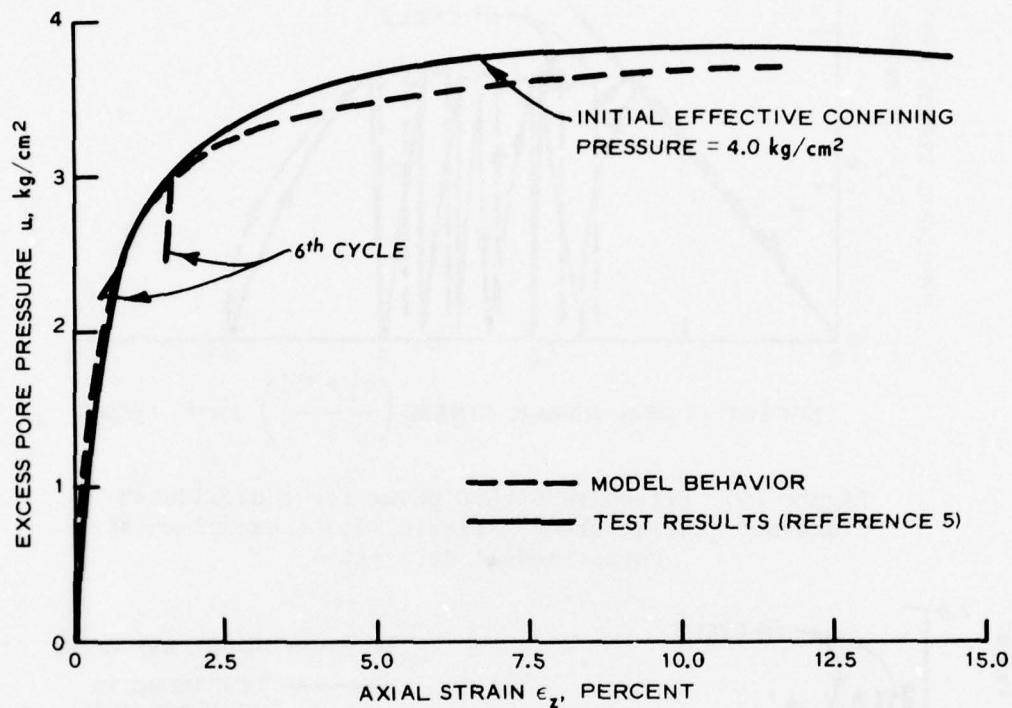


Figure 31. Excess pore water pressure versus axial strain response from cycled undrained triaxial test; experimental versus model; data set 4

## PART VI: SUMMARY AND RECOMMENDATIONS

36. A three-dimensional elastic-plastic isotropic constitutive relation has been developed for simulating the stress-strain-pore pressure response of saturated cohesionless materials. The major new features of the constitutive model are (a) its treatment of work-softening behavior, and (b) its ability to predict progressive increases of pore pressure under low-amplitude (subfailure) cyclic shear loadings. Both of these phenomena are important factors that contribute to the liquefaction of saturated sands. The constitutive relation also allows for dependency of the elastic shear modulus on the shearing stress and plastic volumetric strain. This particular feature of the model is quite useful for simulating the nonlinear shearing stress-strain response of soils.

37. The formulation of the work-softening behavior is numerically stable. Theoretically, however, this behavior could violate the Drucker<sup>6</sup> stability postulate, which is a sufficient, though not necessary, condition for satisfying all of the thermodynamic and continuity requirements of the incremental theory of plasticity.

38. It is recommended that Phase III of this investigation include incorporation of this constitutive model into a suitable numerical computer code for use in the assessing of the liquefaction potential of dams and other earth structures subjected to different transient or static-type loadings.

#### REFERENCES

1. Baladi, G. Y. and Rohani, B., "Liquefaction Potential of Dams and Foundation; Development of an Elastic-Plastic Constitutive Relationship for Saturated Sand," Research Report S-76-2, Report 3, Feb 1977, U. S. Army Engineer Waterways Experiment Station, CE, Vicksburg, Miss.
2. Schofield, A. N. and Wroth, P., Critical State Soil Mechanics, McGraw-Hill, New York, 1968.
3. Sandler, I. S., DiMaggio, F. L., and Baladi, G. Y., "Generalized Cap Model for Geological Materials," Journal, Geotechnical Engineering Division, American Society of Civil Engineers, Vol 102, No. GT7, Jul 1976, pp 683-699.
4. Townsend, F. C. and Mulilis, J. P., "Liquefaction Potential of Sands Under Static and Cyclic Loading" (in preparation), U. S. Army Engineer Waterways Experiment Station, CE, Vicksburg, Miss.
5. Castro, G., "Liquefaction of Sands," Harvard University Soil Mechanics Series, Pierce Hall, Cambridge, Mass., No. 81, 1969.
6. Drucker, D. C., "On Uniqueness in the Theory of Plasticity," Quarterly of Applied Mathematics, Vol 14, 1956, pp. 35-42.
7. Handleman, G. H. et al., "On the Mechanical Behavior of Metals in the Strain-Hardening Range," Quarterly of Applied Mathematics, Vol 4, 1947, pp 397-407.

Table 1

Numerical Values of Material Constants for  
Reid-Bedford Model Sand and Banding Sand

Material Constraints	Unit of Measure	Reid-Bedford Model Sand		Banding Sand	
		Relative Density 20% (Data Set 1)	Relative Density 76% (Data Set 2)	Relative Density 13% (Data Set 3)	Relative Density 21% (Data Set 4)
$K_i$	$\text{kg/cm}^2$	300.0	300.0	500.0	1200.0
$K_L$	-1	0.85	0.7	0.5	0.0
$K_2$	$(\text{kg/cm}^2)$	0.1	0.25	6.0	0.0
$G_i$	$\text{kg/cm}^2$	160.0	60.0	100.0	550.0
$G_L$	-1	0.8	0.8	0.8	0.0
$G_2$	$(\text{kg/cm}^2)$	0.6	0.075	6.0	0.0
$G_3$	$\text{kg/cm}^2$	0.0	100.0	0.0	0.0
$G_4$		0.0	$1.0 \times 10^5$	0.0	0.0
$k$	$\text{kg/cm}^2$	0.0	0.0	0.0	0.0
$\alpha$		0.2309	0.3	0.2533	0.2533
$W$	-1	0.0075	0.0055	0.3	0.03
$D$	$(\text{kg/cm}^2)$	0.14	0.14	0.1	0.15
$R_i$		4.33	1.0	8.0	7.25
$R_L$	-1	0.0	0.0	0.0	0.0
$R_2$	$(\text{kg/cm}^2)$	0.0	0.0	0.0	0.0



APPENDIX A: FUNDAMENTAL EQUATIONS OF ELASTIC-PLASTIC  
MATERIAL MODELS

Basic Concepts from Continuum Mechanics

1. In engineering practice it is convenient, and often reasonable, to disregard the structural details of materials and consider their gross behavior only. Engineering materials are therefore described, or characterized, mathematically within the frameworks of the theory of continuous mass media. Neglecting thermal effects, the basic field equations that govern the motion of a continuum are the continuity equation\*

$$\frac{\partial \rho}{\partial t} + (\rho v_i)_{,i} = 0 \quad (A1)$$

and the equations of motion

$$\sigma_{ij,j} + F_i - \rho a_i = 0 \quad (A2)$$

where

$\rho$  = mass density

$t$  = time

$v_i$  = components of velocity vector

$\sigma_{ij}$  = symmetrical stress tensor

$F_i$  = components of body force

$a_i$  = components of acceleration vector

2. Equations A1 and A2 constitute four equations that involve ten unknown functions of time and space: The mass density  $\rho$ , the three velocity components  $v_i$ , and the six independent stress components  $\sigma_{ij}$ . The body force components  $F_i$  are known quantities and the acceleration components  $a_i$  are expressible in terms of the velocity

---

\* Indices assume values 1, 2, or 3. A repeated index is to be summed over its range. A comma in the subscripts represents a derivative. Quantities are referred to rectangular Cartesian coordinates  $X_i$ .

components  $v_i$ . Therefore, six additional equations relating the ten unknown variables are required in order to determine the motion or deformation of a medium when subjected to external disturbances such as surface forces and/or displacements. In continuum mechanics, such relations are stated by constitutive equations (or material models) which relate stresses to deformation and history of deformation. The difference between constitutive equations and field equations (Equations A1 and A2) is that the latter are applicable to all materials, whereas the former represent the intrinsic response of a particular material or class of materials.

3. The general form of a constitutive equation may be expressed by the functional form

$$g_{ab} (D_{mn}, \epsilon_{rs}, \Omega_{qp}, \sigma_{ij}, \rho) = 0 \quad (A3)$$

where the deformation-rate and spin tensors,  $D_{mn}$  and  $\Omega_{qp}$ , respectively, are related to the components of the velocity vector  $v_i$

$$D_{mn} = \frac{1}{2} (v_{m,n} + v_{n,m})$$

$$\Omega_{pq} = \frac{1}{2} (v_{p,q} - v_{q,p}) \quad (A4)$$

and the strain tensor  $\epsilon_{rs}$  is related to the components of the displacement vector  $u_i$ . For small displacement gradients,

$$\epsilon_{rs} = \frac{1}{2} (u_{r,s} + u_{s,r}) \quad (A5)$$

Equations A1 through A3 constitute ten equations which include ten unknown variables. These equations will lead, in conjunction with the kinematic relations given by Equations A4 and A5 and boundary conditions, to a complete description for solution of a boundary-value problem.

4. The mechanical behavior of a number of engineering materials is described within the framework of elastic-plastic constitutive

relationships. The development of the specific functional form of Equation A3 for the elastic-plastic models is given in the following section.

#### General Description of Elastic-Plastic Constitutive Models

5. The basic premise of elastic-plastic constitutive models is the assumption that certain materials are capable of undergoing small plastic (permanent) as well as elastic (recoverable) strains at each loading increment. Mathematically, the total strain increment is assumed to be the sum of the elastic and plastic strain increments; i.e.,

$$d\epsilon_{ij} = d\epsilon_{ij}^E + d\epsilon_{ij}^P \quad (A6)$$

where

$d\epsilon_{ij}$  = components of the total strain increment tensor

$d\epsilon_{ij}^E$  = components of the elastic strain increment tensor

$d\epsilon_{ij}^P$  = components of the plastic strain increment tensor

6. Within the elastic range the behavior of the material can be described by an elastic constitutive relation of the type

$$d\epsilon_{ij}^E = A_{ijkl} (\sigma_{mn}) d\sigma_{kl} \quad (A7)$$

where

$A_{ijkl}$  = material response function

$d\sigma_{kl}$  = components of stress increment tensor

The behavior of the material in the plastic range can be described within the framework of the generalized incremental theory of plasticity. The mathematical basis of the theory was established by Drucker<sup>6\*</sup> by

---

\* Raised numerals refer to similarly numbered items in the References at the end of the main text.

introducing the concept of material stability with the following implications:

- a. Yield surface (loading function) should be convex in stress space.
- b. Yield surface and plastic potential should coincide (this is referred to as associated flow rule).
- c. Work "softening" should not occur.

These three conditions can be summarized mathematically by the following inequality:

$$d\sigma_{ij} \, d\epsilon_{ij}^P \geq 0 \quad (A8)$$

The above conditions allow considerable flexibility in choosing the form of the loading function  $\delta$  for the model, which serves as both a yield surface and plastic potential. For isotropic materials the yield surface may be expressed, for example, as

$$\delta \left( J_1, \sqrt{J_2}, \kappa \right) = 0 \quad (A9)$$

where

$J_1 = \sigma_{nn}$  = first invariant of stress tensor

$\bar{J}_2 = \frac{1}{2} S_{ij} S_{ij}$  = second invariant of stress deviation tensor

$S_{ij} = \sigma_{ij} - (J_1/3)\delta_{ij}$  = stress deviation tensor

$\delta_{ij} = \begin{cases} 1 & i = j \\ 0 & i \neq j \end{cases}$  = Kronecker delta

$\kappa$  = a hardening parameter

The hardening parameter  $\kappa$ , in general, can be taken to be a function of the plastic strain tensor  $\epsilon_{ij}^P$ . The yield surface of Equation A9 may expand or contract as the hardening parameter  $\kappa$  increases or decreases, respectively (Figure A1).

7. Conditions a, b, and c above, taken in conjunction with Equation A9, result in the following plastic flow rule for isotropic materials:



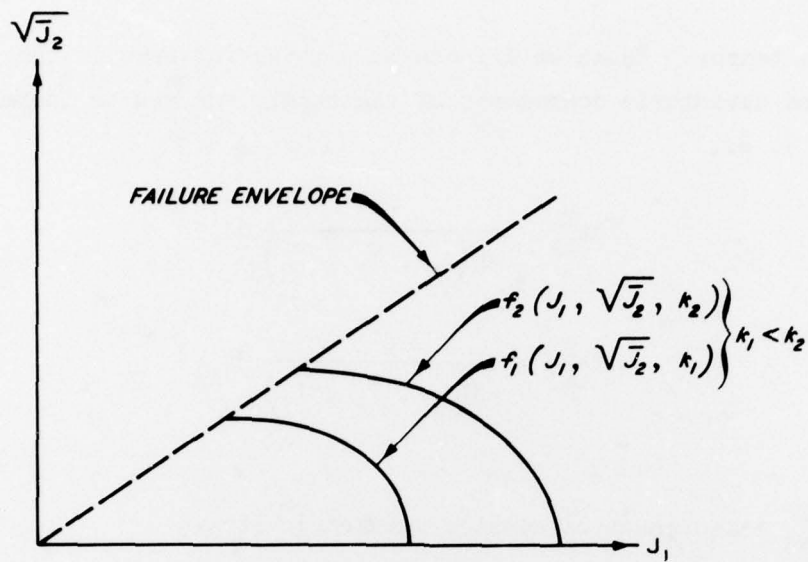


Figure A1. Typical yield surface for an elastic-plastic model

$$d\epsilon_{ij}^P = \begin{cases} d\lambda \frac{\partial \phi}{\partial \sigma_{ij}} & \text{if } \phi = 0 \\ 0 & \text{if } \phi < 0 \end{cases} \quad (A10)$$

where  $d\lambda$  is a positive scalar factor of proportionality, which is non-zero only when plastic deformations occur, and is dependent on the particular form of the loading function.

#### Elastic strain increment tensor

8. For isotropic elastic materials the strain increment tensor (Equation A7) takes the following form:

$$d\epsilon_{ij}^E = \frac{\delta_{ij}}{9K} dJ_1 + \frac{1}{2G} dS_{ij} \quad (A11)$$

The bulk and shear moduli can be functions of the invariants of the stress tensor. Accordingly, assume that  $K = K(J_1, \bar{J}_2, \bar{J}_3)$  and  $G = G(J_1, \bar{J}_2, \bar{J}_3)$ , where  $\bar{J}_3$  is the third invariant of the stress

deviation tensor. Equation A11 can be written in terms of the hydrostatic and deviatoric components of the strain and stress increment tensors; i. e.,

$$d\epsilon_{kk}^E = \frac{1}{3K(J_1, \bar{J}_2, \bar{J}_3)} dJ_1 \quad (A12)$$

$$de_{ij}^E = \frac{1}{2G(J_1, \bar{J}_2, \bar{J}_3)} dS_{ij} \quad (A13)$$

where

$d\epsilon_{kk}^E$  = increment of elastic volumetric strain

$de_{ij}^E$  = elastic strain deviation increment tensor

In order not to generate energy or hysteresis within the elastic range, the elastic behavior of the model must be path independent. The material should then possess a positive definite elastic internal energy function  $\Psi$ , which is independent of stress path. The strain energy function can be written as

$$\begin{aligned} \Psi &= \int_0^{\epsilon_{ij}} \sigma_{ij} d\epsilon_{ij} \\ &= \int_0^{\sigma_{ij}} \left( S_{ij} + \frac{1}{3} J_1 \delta_{ij} \right) \left[ \frac{dJ_1}{9K(J_1, \bar{J}_2, \bar{J}_3)} \delta_{ij} + \frac{dS_{ij}}{2G(J_1, \bar{J}_2, \bar{J}_3)} \right] \\ &= \int_0^{J_1} \frac{J_1}{9K(J_1, \bar{J}_2, \bar{J}_3)} dJ_1 + \int_0^{S_{ij}} \frac{1}{2G(J_1, \bar{J}_2, \bar{J}_3)} S_{ij} dS_{ij} \\ &= \int_0^{J_1} \frac{d(J_1)^2}{18K(J_1, \bar{J}_2, \bar{J}_3)} + \int_0^{\bar{J}_2} \frac{d\bar{J}_2}{2G(J_1, \bar{J}_2, \bar{J}_3)} \end{aligned} \quad (A14)$$

In order for  $\Psi$  to be independent of stress path, the integrals in Equation A14 have to depend only on the current values of  $J_1$  and  $\bar{J}_2$ .

Therefore, the bulk and shear moduli have to be expressed as

$$\begin{aligned} K &= K(J_1) \\ G &= G(\bar{J}_2) \end{aligned} \quad (A15)$$

Further,  $K$  and  $G$  must always be positive. Since during elastic deformation the hardening parameter  $\kappa$  is constant, the bulk and shear moduli can also be expressed as

$$\begin{aligned} K &= K(J_1, \kappa) \\ G &= G(\bar{J}_2, \kappa) \end{aligned} \quad (A16)$$

#### Plastic strain increment tensor

9. The plastic strain increment tensor is given by Equation A10 where the loading function  $\phi$  is given by Equation A9. The hardening function in Equation A9 could be taken as being equal to plastic volumetric strain  $\epsilon_{kk}^P$ ; thus

$$\kappa = \epsilon_{kk}^P \quad (A17)$$

The use of Equation A17 will allow the yield surface to expand as well as to contract, Figure A1. The plastic loading criteria for the function  $\phi$  are given as

$$\frac{\partial \phi}{\partial \sigma_{ij}} d\sigma_{ij} \begin{cases} > 0 \text{ loading} \\ = 0 \text{ neutral loading} \\ < 0 \text{ unloading} \end{cases} \quad (A18)$$

Because  $d\epsilon_{ij}^P = 0$  during unloading or neutral loading, as well as for  $\phi < 0$ , Equations A11 through A13 are used to determine the purely elastic strain changes. The prescription that neutral loading produces no plastic strain is called the continuity condition. Its satisfaction

leads to coincidence of elastic and plastic constitutive laws during neutral loading.<sup>6,7</sup>

10. Like the elastic behavior, the plastic stress-strain relation can be expressed in terms of the hydrostatic and deviatoric components of strain. Application of the chain rule of differentiation to the right side of Equation A10 yields

$$d\epsilon_{ij}^P = d\lambda \left( \frac{\partial \phi}{\partial J_1} \frac{\partial J_1}{\partial \sigma_{ij}} + \frac{\partial \phi}{\partial \sqrt{J_2}} \frac{\partial \sqrt{J_2}}{\partial \sigma_{ij}} \right)$$

or

$$d\epsilon_{ij}^P = d\lambda \left( \frac{\partial \phi}{\partial J_1} \delta_{ij} + \frac{1}{2\sqrt{J_2}} \frac{\partial \phi}{\partial \sqrt{J_2}} S_{ij} \right) \quad (A19)$$

Multiplication of both sides of Equation A19 by  $\delta_{ij}$  gives

$$d\epsilon_{kk}^P = 3 d\lambda \frac{\partial \phi}{\partial J_1} \quad (A20)$$

The deviatoric component of the plastic strain increment tensor ( $d\epsilon_{ij}^P$ ) can be written as

$$d\epsilon_{ij}^P = d\epsilon_{ij}^P - \frac{1}{3} d\epsilon_{kk}^P \delta_{ij} \quad (A21)$$

Substitution of Equation A19 and A20 into Equation A21 yields

$$d\epsilon_{ij}^P = \frac{d\lambda}{2\sqrt{J_2}} \frac{\partial \phi}{\partial \sqrt{J_2}} S_{ij} \quad (A22)$$

11. In order to use Equations A20 and A22, or Equation A19, the proportionality factor  $d\lambda$  must be determined. This can be accomplished in the following manner. From Equations A9 and A17 the total derivative of  $\phi$  becomes

$$d\phi = \frac{\partial \phi}{\partial J_1} dJ_1 + \frac{1}{2\sqrt{J_2}} \frac{\partial \phi}{\partial \sqrt{J_2}} S_{ij} dS_{ij} + \frac{\partial \phi}{\partial \epsilon_{kk}^P} d\epsilon_{kk}^P = 0 \quad (A23)$$



In view of Equations A12, A13, and A20, Equation A23 becomes

$$3K d\epsilon_{kk}^E \frac{\partial \delta}{\partial J_1} + \frac{G de_{ij}^E}{\sqrt{J_2}} \frac{\partial \delta}{\partial \sqrt{J_2}} S_{ij} + 3 d\lambda \frac{\partial \delta}{\partial J_1} \frac{\partial \delta}{\partial \epsilon_{kk}^P} = 0 \quad (A24)$$

Substitution of Equation A6 into Equation A24 results in

$$3K (d\epsilon_{kk} - d\epsilon_{kk}^P) \frac{\partial \delta}{\partial J_1} + \frac{G}{\sqrt{J_2}} (de_{ij} - de_{ij}^P) \frac{\partial \delta}{\partial \sqrt{J_2}} S_{ij} = -3 d\lambda \frac{\partial \delta}{\partial J_1} \frac{\partial \delta}{\partial \epsilon_{kk}^P} \quad (A25)$$

or

$$3K d\epsilon_{kk} \frac{\partial \delta}{\partial J_1} + \frac{G}{\sqrt{J_2}} \frac{\partial \delta}{\partial \sqrt{J_2}} S_{ij} de_{ij} = 3K d\epsilon_{kk}^P \frac{\partial \delta}{\partial J_1} + \frac{G}{\sqrt{J_2}} \frac{\partial \delta}{\partial \sqrt{J_2}} S_{ij} de_{ij}^P - 3 d\lambda \frac{\partial \delta}{\partial J_1} \frac{\partial \delta}{\partial \epsilon_{kk}^P} \quad (A26)$$

With the substitution of the values of  $d\epsilon_{kk}^P$  and  $de_{ij}^P$  from Equations A20 and A22, respectively, Equation A26 becomes

$$3K d\epsilon_{kk} \frac{\partial \delta}{\partial J_1} + \frac{G}{\sqrt{J_2}} \frac{\partial \delta}{\partial \sqrt{J_2}} S_{ij} de_{ij} = 9K d\lambda \left( \frac{\partial \delta}{\partial J_1} \right)^2 + G d\lambda \left( \frac{\partial \delta}{\partial \sqrt{J_2}} \right)^2 - 3 d\lambda \frac{\partial \delta}{\partial J_1} \frac{\partial \delta}{\partial \epsilon_{kk}^P} \quad (A27)$$

When the equation is solved for  $d\lambda$ , it is expressed as\*

$$d\lambda = \frac{3K \frac{\partial \delta}{\partial J_1} d\epsilon_{kk} + \frac{G}{\sqrt{J_2}} \frac{\partial \delta}{\partial \sqrt{J_2}} S_{ij} de_{ij}}{9K \left( \frac{\partial \delta}{\partial J_1} \right)^2 + G \left( \frac{\partial \delta}{\partial \sqrt{J_2}} \right)^2 - 3 \frac{\partial \delta}{\partial J_1} \frac{\partial \delta}{\partial \epsilon_{kk}^P}} \quad (A28)$$

---

\* For elastic-ideally plastic material, the numerator in Equation A28 is  $d\delta$  and  $\partial \delta / \partial \epsilon_{kk}^P = 0$ .

Total strain increment tensor

12. The total strain increment tensor can be obtained by combination of Equations A6, A11, A19, and A28; thus,

$$d\epsilon_{ij} = \frac{dJ_1}{9K} \delta_{ij} + \frac{dS_{ij}}{2G} + \left[ \frac{3K \frac{\partial \phi}{\partial J_1} d\epsilon_{kk} + \frac{G}{\sqrt{J_2}} \frac{\partial \phi}{\partial \sqrt{J_2}} S_{mn} de_{mn}}{9K \left( \frac{\partial \phi}{\partial J_1} \right)^2 + G \left( \frac{\partial \phi}{\partial \sqrt{J_2}} \right)^2 - 3 \frac{\partial \phi}{\partial J_1} \frac{\partial \phi}{\partial \epsilon_{kk}^P}} \right] \times \left( \frac{\partial \phi}{\partial J_1} \delta_{ij} + \frac{1}{2\sqrt{J_2}} \frac{\partial \phi}{\partial \sqrt{J_2}} S_{ij} \right) \quad (A29)$$

Similarly, the stress increment tensor can be written as

$$d\sigma_{ij} = K d\epsilon_{kk} \delta_{ij} + 2G de_{ij} - \left[ \frac{3K \frac{\partial \phi}{\partial J_1} d\epsilon_{kk} + \frac{G}{\sqrt{J_2}} \frac{\partial \phi}{\partial \sqrt{J_2}} S_{mn} de_{mn}}{9K \left( \frac{\partial \phi}{\partial J_1} \right)^2 + G \left( \frac{\partial \phi}{\partial \sqrt{J_2}} \right)^2 - 3 \frac{\partial \phi}{\partial J_1} \frac{\partial \phi}{\partial \epsilon_{kk}^P}} \right] \times \left( 3K \frac{\partial \phi}{\partial J_1} \delta_{ij} + 2G \frac{\partial \phi}{\partial \sqrt{J_2}} \frac{S_{ij}}{2\sqrt{J_2}} \right) \quad (A30)$$

Equation A29, or Equation A30, is the general constitutive equation for an elastic-plastic isotropic material. To use these equations it is only necessary to specify the functional forms of  $K$ ,  $G$ , and  $\phi$ .

## APPENDIX B: NOTATION

$a_i$	Components of acceleration vector
$A_{ijkl}$	Material response function
$de_{ij}^E$	Elastic strain deviation increment tensor
$de_{ij}$	Components of the total strain increment tensor
$de_{ij}^E$	Components of the elastic strain increment tensor
$de_{kk}^E$	Increment of elastic volumetric strain
$de_{ij}^P$	Components of the plastic strain increment tensor
$de_{kk}^P$	Increment of plastic volumetric strain
$d\lambda$	Positive scalar factor of proportionality used with flow rule
$d\sigma_{ij}$	Components of stress increment tensor
$D$	Material constant
$D_{mn}$	Deformation rate tensor
$e$	Void ratio
$f(J_1', \sqrt{J_2})$	Failure envelope portion of the loading function
$f$	Loading function
$F_i$	Components of body force
$G$	Elastic shear modulus
$G_i$	Initial elastic shear modulus
$G_1, G_2, G_3, G_4$	Material constants
$J_1'$	First invariant of effective stress tensor
$\bar{J}_2$	Second invariant of the stress deviation tensor
$\bar{J}_3$	Third invariant of the stress deviation tensor
$k$	Material constant representing cohesive strength of material
$K$	Elastic bulk modulus
$\tilde{K}$	Apparent bulk modulus of material
$K_i$	Initial elastic bulk modulus
$K_1, K_2$	Material constants
$P'$	Effective pressure or effective mean normal stress

$P'_c$	Confining pressure at end of isotropic consolidation phase
$R$	Ratio of the major to the minor axis of the elliptic yield surface
$R_f$	Change in $R$ during cyclic loading
$R_i, R_1, R_2$	Material constants
$S_{ij}$	Stress deviation tensor
$t$	Time
$u$	Excess pore pressure
$u_i$	Components of displacement vector
$v_i$	Components of velocity vector
$W$	Material constant, maximum nonrecoverable volumetric compaction material can withstand under isotropic consolidation
$z, r, \theta$	Cylindrical coordinate system
$\alpha$	Material constant representing frictional strength of material
$\Delta V/V$	Volumetric strain
$\delta_{ij}$	Kronecker delta
$\epsilon_{ij}$	Strain tensor
$\epsilon_{kk}$	Volumetric strain
$\epsilon_r$	Radial strain
$\epsilon_z$	Axial strain
$\epsilon_\theta$	Tangential strain components
$\epsilon_{kk}^p$	Plastic volumetric strain
$\kappa$	Hardening parameter
$\rho$	Mass density
$\sigma_{ij}$	Total stress tensor
$\sigma'_{ij}$	Effective stress tensor
$\sigma_r$	Radial total stress component
$\sigma_z$	Axial stress component
$\sigma_\theta$	Tangential total stress component
$\psi$	Complementary energy density function
$\Omega_{qp}$	Spin tensor



In accordance with letter from DAEN-RDC, DAEN-ASI dated 22 July 1977, Subject: Facsimile Catalog Cards for Laboratory Technical Publications, a facsimile catalog card in Library of Congress MARC format is reproduced below.

Baladi, George Youssef

Liquefaction potential of dams and foundations; Report 5: Development of a constitutive relation for simulating the response of saturated cohesionless soil / by George Y. Baladi, Behzad Rohani. Vicksburg, Miss. : U. S. Waterways Experiment Station ; Springfield, Va. : available from National Technical Information Service, 1978.

46, [13] p. : ill. ; 27 cm. (Research report - U. S. Army Engineer Waterways Experiment Station : S-76-2, Report 5)

Prepared for Office, Chief of Engineers, U. S. Army, Washington, D. C., under CWIS 31145.

References: p. 46.

1. Cohesionless soils. 2. Constitutive models. 3. Dams. 4. Foundations. 5. Hysteresis. 6. Liquefaction (Soils). 7. Saturated soils. 8. Stress-strain relations. I. Rohani, Behzad, joint author. II. United States. Army. Corps of Engineers. III. Series: United States. Waterways Experiment Station, Vicksburg, Miss. Research report ; S-76-2, Report 5. TA7.W34r no.S-76-2 Report 5